Structural diagenesis in ultra-deep tight sandstones in Kuqa depression, Tarim Basin, China

Jin Lai[1,2], Dong Li[1], Yong Ai[3], Hongkun Liu[1], Deyang Cai[3], Kangjun Chen[1], Yuqiang Xie[1], Guiwen Wang[1,2]

1. State Key Laboratory of Petroleum Resources and Prospecting, China University of Petroleum (Beijing), Beijing 102249, China

2. College of Geosciences, China University of Petroleum (Beijing), Beijing 102249, China

3. Research Institute of Petroleum Exploration and Development, Tarim Oilfield Company, CNPC, Korla 841000, Xinjiang, China

Corresponding author: Jin Lai, China University of Petroleum (Beijing), 18 Fuxue Road, Changping, Beijing, China 102249. Tel.: +861089733435; Fax.: +861089734158; **E-mail**: sisylaijin@163.com

Guiwen Wang, China University of Petroleum (Beijing), **E-mail**: wanggw@cup.edu.cn

ABSTRACT:

The Lower Cretaceous Bashijiqike Formation of Kuqa depression is ultra-deeply buried sandstones in fold-and-thrust belts. Few researches have linked diagenetic processes with structure. To fill this gap, a comprehensive analysis integrating diagenesis with structure pattern, fracture and in situ stress is performed following a structural diagenetic approach.

The results show that the pore spaces include residual intergranular pores, intergranular and intragranular dissolution pores, and micro-fractures. The sandstones experienced a high degree of mechanical compaction, but compaction is limited in well-sorted rocks or abundant in rigid quartz grains. The most volumetrically important diagenetic minerals are calcites. The framework grains experienced a varied degree of dissolution, and intergranular and intragranular dissolution pores are formed. Special aims are paid on the dissolution associated with the fracture planes. Large numbers of natural fractures are cemented by carbonate cements, which limit fluid flow. In addition, the presences of fracture enhance dissolution, and the fracture planes are enlarged by dissolution. Cementation and dissolution can occur simultaneously in fracture surfaces, and the enlarged fracture surfaces can be cemented by late-stage cements. The in situ stress magnitudes are calculated using well logs. The horizontal stress difference ($\Delta\sigma$) determines the degree of mechanical compaction, and rocks associated with low $\Delta\sigma$ experienced a low degree of compaction, and there contain preserved intergranular pores. Natural fractures are mainly related to the low $\Delta\sigma$ layers. The presences of intergranular and intragranular dissolution pores are mainly associated with the fractured zones. The high quality reservoirs with intergranular pores or fractures are related to low $\Delta\sigma$ layers. The structural diagenesis researches above help the prediction of reservoir quality in ultra-deep sandstones, and reduce the uncertainty in deep natural gas exploration in Kuqa depression.

Key words: Structural diagenesis; fracture; in situ stress; diagenesis; Kuqa depression; ultra-deep sandstone

1. Introduction

The Kuqa depression is a foreland depression experienced multistage tectonic evolutions during Mesozoic to Cenozoic periods, consequently many high and steep thrust faults and fault-related folds were formed (Feng et al., 2018; Neng et al., 2018; Lai et al., 2019a). In addition, the dominant gas bearing Lower Cretaceous Bashijiqike Formation is buried to an ultra-deep depth of 5500-8000m (Lai et al., 2019a). The ultra-deep burial depths, complex structure patterns and concentrated stress will result in complex diagenetic modifications and pore evolution histories (Laubach et al., 2010; Wu et al., 2019; Del Sole et al., 2020). Previous studies have individually unraveled the structural evolution, in situ stress, fracture as well as diagenesis of Bashijiqike Formation in Kuqa depression (Jia and Li, 2008; Lai et al., 2017a; Shen et al., 2017; Nian et al., 2018; Ju and Wang, 2018; Lai et al., 2019a). Despite the extensive researches on diagenesis and structure, few researches have been conducted on the structural diagenesis by interacting structure with diagenesis.

Structural diagenesis, a cross-disciplinary approach investigating relationships between structures (deformation, fractures, etc) and diagenesis (Laubach et al., 2010), helps to better understand the changes in reservoir petrophysical properties and subsurface fluid flow (Vandeginste et al., 2012; Matonti et al., 2017; Ferraro et al., 2019; Wu et al., 2019; Rodrigues et al., 2021). Foreland fold-and-thrust belts are challenging for hydrocarbon exploration due to their structural complexity and heterogeneous reservoir quality distribution (Vandeginste et al., 2012). Actually the structural complexity highly impacts fluid flow and diagenetic processes (Vandeginste et al., 2012; Wang et al., 2021). The impact of diagenesis and diagenetic minerals on reservoir quality are well described (Lai et al., 2017a), while little is known about the fracture-induced diagenesis, which is present throughout the entire Bashijiqike formation. Therefore the comprehensive structural diagenesis analysis in Kuqa depression is of great scientific and practical significances.

This study is focused on linking diagenesis to structural complexity, and is organized as: 1) to describe the lithology and pore spaces; 2) to unravel the type and degree of diagenesis and diagenetic minerals; 3) to characterize the fracture using core and image logs; 4) to unravel the dissolution and cementation along the fracture surfaces; 5) to calculate the in situ stress magnitudes; 6) to describe the in situ stress, compaction and preservation of intergranular pores, as well as the fracture enhanced dissolution; 7) to unravel the diagenesis (preservation of intergranular pores, formation of dissolution pores, and fracture) within the structural complexity. Results of this study are hoped to better understand the structural and diagenetic processes, and reduces the uncertainty for reservoir quality prediction of ultra-deep sandstones in Kuqa depression and similar basins worldwide.

2. Geological Settings

The Kuqa depression is located in the North Tarim Basin, West China (Fig.1A, 1B). The petroliferous Tarim Basin is located between the Tianshan and Kunlun Mountains, and occupies an area of 56×10^4 km^2 (Fig.1A) (Jin et al., 2008; Qiu et al., 2012; Gao et al., 2016; Jiang et al., 2016; Fu, 2019; Lai et al., 2021a). The Kuqa depression experienced a long and complex evolutionary history during the Mesozoic to Cenozoic time, forming two sags and three structural belts: Baicheng and Yangxia Sag, northern monocline, Kelasu and Qilitage structural belts (Lai et al., 2015; Shen et al., 2017; Feng et al., 2018; Ju and Wang, 2018).

Large numbers of thrust faults and fault related folds, which act as structural traps for oil and gas in the Kuqa depression (Fig.1C), were formed due to the multistage tectonic activity and strength tectonic stress (Zhang and Huang, 2005; Zeng et al., 2010; Nian et al., 2016; Feng et al., 2018; Zheng et al., 2020). Four wellblocks are recognized in the Kelasu structural belts, and they include Bozi, Dabei, Keshen and Kela well blocks (Fig.1C).

The Mesozoic and Cenozoic strata are over 10, 000m thickness (Chen et al., 2000; Zou et al., 2006). There contains a well-developed reservoir-cap rock assemblage in the Kuqa depression (Jin et al., 2008). Among them, the Lower Cretaceous Kapushaliang Group (K_1kp) and Bashijiqike Formation (K_1bs) are the dominant reservoir intervals, and many giant gas fields including Kela 2, Awa, Bozi, Dina, Dabei, Keshen gas fields have been discovered in this gas bearing formation (Fig.1C) (Jin et al., 2008; Shen et al., 2017; Nian et al., 2018). The overlying Kumugeliemu group ($E_{1\text{-}2}km$) acts as the regional cap rocks in the Kuqa depression due to the favorable cap property of the thick-layer gypsum salt rocks (Fig.1C). Additionally, the underlying Triassic-Jurassic coal bearing formations (Jurassic Yangxia formation (J_1y), Triassic Karamay (T_2k) and Huangshanjie (T_3h) formations) are the source rocks in Kuqa depression (Zhao et al., 2005; Shen et al., 2017).

The Lower Cretaceous Bashijiqike Formation is divided into three members (K_1bs_3, K_1bs_2 and K_1bs_1 member) from bottom to top. Depositional facies of the Bashijiqike Formation are recognized as fan-braided deltaic environments (Jia and Li, 2008) (Fig.2). The lithologies include a wide range from siltstone, fine-medium grained sandstone, to pebby sandstone and conglomerate (Zeng et al., 2020) (Fig.2), and intergranular, intragranular pores as well as fracture constitute the main reservoir pore spaces (Nian et al., 2018; Lai et al., 2019a; Nian et al., 2021). The depositional subfacies evolved from fan delta plain in K_1bs_3 to braided delta front subfacies in K_1bs_2 and K_1bs_1 members, and the main depositional microfacies recognized include distributary channel, mouth bar and distributary bay (Wang et al., 2013; Lai et al., 2017a; Nian et al., 2018).

3. Data and methods

Cores were taken from 18 cored wells, and photos were taken for each species of core. In addition, almost all the examined cores were slabbed 360° to better show the distinct characteristics of core surfaces.

Approximately 200 thin sections were polished to approximately 0.03 mm and impregnated with blue resin to highlight porosity. Thin sections were also stained with mixed Alizarin Red S and potassium ferricyanide solution for differentiating various types of carbonate minerals (calcite, dolomite and their ferroan equivalents).

Thin sections were firstly examined by optical transmitted light and subsequently Cathodoluminescence (CL) microscopy. The CL observations were made using a ORTHOPLAN cold cathode device.

SEM (scanning electron microscope) was used to detect the various types of clay minerals and recognize the micropores within clay minerals. The secondary electron images were used to detect the pores and clay minerals associated with the freshly broken rock surfaces.

Conventional well logs include three lithology logs including calipers (CAL), Gamma ray (GR), Spontaneous Potential (SP); three porosity logs including sonic transic time (AC) and compensated neutron log (CNL), and bulk density (DEN); deep and shallow lateral resistivity logs (LLD, LLS).

Schlumberger's FMI (Fullbore Formation MicroImager) image logs were used to obtain the high resolution (5 mm) borehole images. A series of data processes including speed correction, eccentering correction, and normalization were used to generate the static and dynamic images. Beddings, natural and induced fractures are manually picked out on the image logs by fitting sinusoidal waves (Lai et al., 2018; Nian et al., 2021).

4. Results

4.1. Lithology and pore systems

The lithologies of the Cretaceous Bashijiqike Formation in Kuqa depression include a wide ranges from conglomerate (Fig.3A), pebby sandstone (Fig.3B), fine-medium grained sandstone (Fig.3C-3D), siltstone (Fig.3E-3F), and mudstone (Fig.3G-3H), indicating a fan-braided deltaic environment (Jia and Li, 2008; Wang et al., 2013; Lai et al., 2018).

The pore spaces include residual intergranular pores with irregular morphology (Fig.4A, 4B), intergranular and intragranular dissolution pores (Fig.4C, 4D) due to dissolved feldspar and rock fragment grains. In some cases, the coexistence of intergranular pores and intragranular dissolution pores is common (Fig.4A-4D). Micro-fracture can also constitute an important pore space (Fig.4E, 4F). Micro-fracture can occur in sandstones with evident intergranular pore spaces (Fig.4E), and they also can be detected in carbonate cemented sandstones (Fig.4F).

4.2. Diagenesis type and degree

The types and degree of diagenetic modification as well as the typical diagenetic minerals in Bashijiqike Formation of Kuqa depression are described in previous studies (Lai et al., 2017a).

The degree of mechanical compaction varied significantly for the Bashijiqike sandstones in the Kuqa depression (Lai et al., 2017a). The sandstones are buried to a great depth from 5500-8000m, and compaction is extensive due to the overburden rocks. The rocks are very heavily compacted especially the very fine-grained or poor sorted rocks (Fig.5A-5B). However, some of the rocks which are well –sorted or abundant in rigid grains can preserve large amounts of intergranular pores (Fig.4A-4B).

In addition, the pore-line grain contacts also suggest a limited degree of compaction, and the cementation is also inhibited (Lai et al., 2019b) (Fig.5C). Actually, there are evident dark cement rims (mixed-layer illite/smectite) on many of the framework grains within these rocks (Fig.4B, 4E), and the presences of authigenic mineral rims on framework grains can inhibit (quartz) cementation into the intergranular pore space (Lai et al., 2017a).

Diagenetic minerals are mainly carbonates, and they are the most volumetrically important (Fig.5D). Carbonate cements, which are in the form of calcites (Fig.5D) and dolomites (Fig.5E), significantly reduce pore spaces. There are even no evident pore spaces in rocks which are extensively cemented by carbonates (Fig.5D, 5E). The CL images prove the extensive carbonate cements in the intergranular pore spaces, and they can even replace framework grains (Fig.5F).

Dissolution occurred along the framework grain boundary and the intragranular pore spaces, forming intergranular and intragranular dissolution pore spaces (Fig.5G, 5H). The dissolution degree is also varied greatly, and significant dissolution is mainly associated with the fine-medium grained rocks (Fig.5G, 5H). The secondary dissolution pores are developed due to framework grains (feldspar and rock fragments) dissolution (Fig.5G, 5H).

There are also minor amount of quartz cements (Fig.5I), and clay minerals in the form of illite and smectite mixed layer (Fig.5J) in the Bashijiqike sandstones of Kuqa depression (Lai et al., 2017a). The quartz cements occur as small authigenic quartz crystals (Fig.5I), while the mixed-layer illite/smectite clays occur as pore filling fibrous or webby morphologies (Fig.5J).

4.3. Compaction, cementation and porosity reduction

Compaction and pore filling cements will reduce porosity in sandstones (Houseknecht et al., 1987; Lima and DeRos, 2002; Mansurbeg et al., 2008; Lai et al., 2015; Haile et al., 2018).

The compactional porosity loss (COPL) is commonly estimated by Eq.(1):

$$COPL = OP - \frac{(100 \times IGV) - (OP \times IGV)}{(100 - IGV)} \quad (1)$$

Where OP is the original porosity (the OP values were estimated as 40% for fine-medium grained, well sorted sandstone), and IGV is the sum of present intergranular porosity and total cement content (intergranular porosity before cementation but after compaction) (Houseknecht et al., 1987; Ozkan et al., 2011; Lai et al., 2015).

The cementational porosity loss (CEPL) can be calculated as Eq.(2) (Houseknecht et al., 1987; Zhang et al., 2008; Ozkan et al., 2011):

$$CEPL = (OP - COPL) \times \frac{CEM}{IGV} \tag{2}$$

Where OP is the original porosity, COPL is compactional porosity loss, and CEM is the total cement volume percentages of rock volume.

The calculated results show that COPL range from 11.8% to 39.6% with an average of 32.0%, while CEPL is in the range from 0 to 27.2%, and averaged as 5.2% (Fig.6). Porosity reduction by mechanical compaction was more significant than by cementation (Fig.6). However, COPL shows no evident relationship with burial depth, and can reach as high as 40% even are shallower buried, and even in depths deeper than 7500m, the COPL can be lower that 20% (Fig.6).

Lai et al. (2017a) has unraveled the paragenetic diagenetic history of the studied rocks, and eogenetic diagenetic mainly include mechanical compaction, precipitation of calcite cements and grain-coating clays, then mesogenetic diagenesis contains framework grain dissolution and precipitation of clay minerals and quartz, while meteoric water of teleodiagenesis results in dissolution of the framework grains.

4.4. Fracture and image log characterization

Natural fractures are important subsurface fluid flow conduits and they play important roles in hydrocarbon accumulation and production (Khoshbakht et al., 2009; Zeng, 2010; Lyu et al., 2016; Lyu et al., 2017; Laubach et al., 2019). In terms of fracture attributes (dip angles), natural fractures can be divided into vertical fractures and high dip angle fractures (>60°), medium dip angle fractures (30°-60°), and low angle fracture (<30°) and horizontal fracture from the aspect of image log interpretation. Additionally, fracture can be classified into open, partly open or closed fractures in terms of fracture status. Core observations show that the fine-medium grained sandstones have the highest abundance of fractures, and open-filled fractures with various dip angles can occur in the fine-medium grained sandstones (Fig.7).

Natural fractures can be easily picked out from the image logs as dark sinusoidal waves in case the drilling muds are conductive (water based drilling muds) (Fig.8) (Ameen et al., 2012; Khoshbakht et al., 2009; Lai et al., 2019a). The continuity of the sinusoidal waves depend on the filling degree of fracture surfaces, i.e., the partly to fully closed fractures (sealed by resistive calcite cements) may show discontinuous to continuous bright sinusoidal waves on the image logs.

Dip direction of fracture can be derived from the lowest point of the sinusoidal waves, while dip angles can be determined by the sine wave amplitudes (Fig.8) (Nie et al., 2013; Keeton, et al., 2015; Lai et al., 2018). Therefore the bedding planes, natural open and closed fractures can be picked out for the entire log intervals. Then rose diagrams of bedding planes, open and closed fractures can be drawn (Lai et al., 2021b) (Fig.9). In addition, four fracture parameters including fracture aperture (FVAH), fracture density (FVDC), fracture porosity (FVPA) and fracture length (FVTL) can be calculated from the image logs (Table.1) (Ameen and Hailwood, 2008; Khoshbakht et al., 2012; Lai et al., 2021b).

Table 1. Image log derived fracture parameters for Well Dabei 1101 in Kuqa depression

Strata	Depth intervals with fractures (m)	Open fractures		Closed fractures		Number of fracture	FVDC (1/m)		FVTL (m)		FVAH (mm)		FVPA (%)	
		Dip angles	Average dip	Dip angles	Average dip		Max	Ave	Max	Ave	Max	Ave	Max	Ave
K_1bs	5790-5800	25°-82°	52°∠144°	40°-50°	45°∠48°	8	2	1.2	3.2	1.7	6	2.6	0.12	0.07
	5801-5802	45°-64°	54°∠234°			6	5	4.1	5.5	4.9	7.9	1.8	0.21	0.14
	5803-5813	39°-72°	52°∠142°			12	3.5	1.7	2.8	2.3	4.2	3.9	0.15	0.08
	5818-5825	41°-59°	46°∠155°			5	1.5	1	2..1	1.5	5.1	3.2	0.16	.0.08
	5827-5845	45°-65°	61°∠137°			8	1.4	0.9	2.5	1.6	2.5	1.2	0.11	0.06
	5869-5888	40°-73°	53°∠133°			21	3.5	1.7	5.4	3.5	8.9	3.8	0.32	0.14
K_1bx	5890-5892	41°-85°	65°∠168°	30°-40°	44°∠56°	7	1.8	1.5	4	3.2	5.6	4.5	0.25	0.15
	5920-5932	45°-70°	56°∠192°			5	1.2	1	1.3	1.1	5.9	2.9	0.29	0.11

4.5. Dissolution and cementation along the fracture surface

Cementation and dissolution within fractures impact fracture patterns and properties (Ukar and Laubach, 2016; Laubach et al., 2019; Baqués et al., 2020). Core observation (including the scanning image of core surfaces) show that the fractures in Bashijiqike sandstones are highly cemented, and the presences of fractures improve subsurface fluid flow (Matonti et al., 2017), and therefore the active fluids rich in Ca^{2+} will be cemented along the fracture surfaces (Fig.10A-10C). No matter high angle, low angle or even horizontal fractures are highly cemented (Fig.10A-10C). Cemented subsurface fractures limit the fluid flow (Laubach et al., 2004; Matonti et al., 2017). In addition, the presence of fracture enhances dissolution, and the fracture surfaces can be observed to be enlarged by dissolution (Fig.10D). In some cases, the cementation and dissolution can occur simultaneously in a fracture surface, and the enlarged fracture surfaces can be fully cemented by the late-stage cements (Fig.10E). Also, in some cases the mudstones can fill the fracture spaces (Fig.10F). Dissolution occurring along the fracture surfaces can even form vugs (Fig.10G-10H), indicating a high degree of dissolved framework grains. However, the dissolved fracture surfaces can in some cases be filled by late-stage carbonate cements (Fig.10G-10H).

Thin section observations also show that the fractures play important roles in enhancing dissolution and cementation (Fig.11A-11C). Calcite cements are commonly detected to occur along the fracture planes, and they can partly to fully fill the fracture spaces (Fig.11A). Also fractures are important channels for fluid flow, and consequently the acids-rich fluids will enhance framework grain dissolution. Therefore, the fracture surfaces are commonly observed to be dissolved (Fig.11B). In some cases, both dissolution and cementation can simultaneously occur along the fracture planes (Fig.11C). The calcite cementation fills the fracture spaces, and reduces fracture effectiveness, while dissolution improves the fracture connectivity (Fig.10; Fig.11). Actually, most opening-mode subsurface fractures contain some amount of cement (Laubach et al., 2018; Bruna et al., 2020).

Vuggy fractures, which were formed due to dissolution along the fracture planes, can also be observed on the image logs, and the fracture surfaces are evidently enlarged (Fig.12). These fractures occur as continuous or discontinuous, conductive, resistive, or mixed (partly resistive and partly conductive) sinusoidal waves on the image logs (Fig.12) (Lai et al., 2018).

4.6. In situ stress direction and magnitudes

4.6.1. In situ stress direction

Determination of the in situ stress direction is important for stress-related geo-hazards and reservoir-related issues (Nian et al., 2016). In situ stress direction can be determined from the induced fractures and borehole breakouts picked out from image logs (Rajabi et al., 2010; Ameen et al., 2012; Nian et al., 2016; Lai et al., 2018). Drilling induced fractures formed as a result of the local stress field around the borehole, and they are parallel to SHmax (present-day maximum horizontal compressive stress) (Wilson et al., 2015). Borehole breakouts are wellbore enlargements induced by in situ stress concentrations, and indicates the orientations of the minimum (Sh_{min}) horizontal stress directions (Bell and Gough, 1979; Zeng and Li, 2009; Massiot et al., 2015; Nian et al., 2016). The trend of the drilling induced fractures is approximately NW-SE direction (Fig.13).

4.6.2. In situ stress magnitudes

The calculation of in situ stress magnitude supports petroleum engineers' decisions about well design, wellbore stability and fracture stimulation (Zoback et al., 2003; Ju and Wang, 2018; Iqbal et al., 2018; Lai et al., 2019a). The three mutually orthogonal principal stresses include (1) vertical (overburden) stress (Sv), (2) maximum horizontal stress (SHmax), and (3) minimum horizontal stress (Shmin) (Zoback et al., 2003; Verweij et al., 2016; Dixit et al., 2017; Lai et al., 2019a).

The magnitudes of SHmax, Shmin and Sv can be determined by constructing 1-D MEMs (one-dimensional mechanical Earth models) (Fig.14) (Zoback et al., 2003; Tingay et al., 2009; Ju et al., 2017; Lai et al., 2019a). The vertical stress is caused by the gravity of overburden rocks (Hassani et al., 2017; Lai et al., 2019a). The magnitude of Sv at a certain depth equals to the weight of overburden rocks, and it can be calculated by Eq.(3) (Verweij et al., 2016; Lai et al., 2019a).

$$S_v = \int_0^H \rho g dz \tag{3}$$

where H is the burial depth, m, ρ is the bulk density, kg/m^3, g is 9.8 m/s^2 (Verweij et al., 2016; Zhang and Zhang, 2017; Ju and Wang, 2018).

Pore pressure (Pp), also is known as formation pressure at a certain depth (Dixit et al., 2017), can be calculated from sonic well logs using Eaton's method (Eaton, 1969; Tingay et al., 2009).

$$P_p = P_0 - (P_0 - P_w)(\Delta t_n / \Delta t)^c \tag{4}$$

where, Pp is the pore pressure (MPa), P_0 (Sv) is the overburden pressure (MPa), Pw is hydrostatic pressure (commonly taken as 9.8 MPa/km), Δt_n is sonic interval transit time at normal pressure, Δt is sonic transit time and c is the coefficient of compaction (Zhang, 2011; Ju et al., 2017).

The determination of the Shmin and SHmax magnitudes via well logs can be calculated based on vertical stress, Poisson's ratio, and pore pressure (Eq.(5), Eq.(6)) (Eaton, 1969; Zhang, 2011; Maleki et al., 2014; Lai et al., 2019a; Zhang et al., 2019). The Shmin will be equal to the SHmax in isotropic stratigraphy (Maleki et al., 2014), however, SHmax is not equal to Shmin in true formation, and the SHmax and Shmin difference (Δσ=SHmax-Shmin) will vary greatly due to presences of major faults and active tectonics (Fig.14) (Maleki et al., 2014; Yeltsov et al., 2014; Ju and Wang, 2018; Lai et al., 2019a).

$$SH_{max} = \frac{\nu}{1-\nu} Sv + \frac{1\text{-}2\nu}{1-\nu} \alpha P_p + \frac{E}{1-\nu^2} \varepsilon_H + \frac{E\nu}{1-\nu^2} \varepsilon_h \quad (5)$$

$$Sh_{min} = \frac{\nu}{1-\nu} Sv + \frac{1\text{-}2\nu}{1-\nu} \alpha P_p + \frac{E}{1-\nu^2} \varepsilon_h + \frac{E\nu}{1-\nu^2} \varepsilon_H \quad (6)$$

where Sv is vertical stress, P_P is pore pressure. E (GPa) is Young's modulus and ν is the Poisson's ratio. α is the Biot's coefficient, which can be obtained on empirical equation. The ε_H and ε_h are the coefficients related to the maximum and minimum horizontal stress magnitudes (Zhang et al., 2019).

5. Discussion

In this section, the impact of in situ stress on compaction will be discussed, and fracture enhanced dissolution in single wells will be linked, and then the variations of fracture-diagenesis within various structure patterns are discussed.

5.1. Compaction and presences of fracture controlled by in situ stress

The horizontal stress difference ($\Delta\sigma$) plays an important role in reservoir quality and fractures (Lai et al., 2019a). The thin section at about depth of 6356 m has abundant intergranular pore spaces, indicating a limited mechanical compaction the rocks experienced. The calculated $\Delta\sigma$ is less than 40 MPa, which is much less than the surrounding rocks (Fig.15). The thin section at about 6420 m depth also indicates a limited mechanical compaction and evident intergranular pores can be observed. The calculated $\Delta\sigma$ is only about 36-39 MPa, indicating a low in-situ stress magnitude. Conversely, the rocks at about 6369 m depth, have experienced an extensive in-situ stress concentration, and the $\Delta\sigma$ can reach as high as 45 MPa (Fig.15). The thin section observation reveals that the rocks have experienced a high degree of compaction, and no evident intergranular pore spaces are observed, and the grains are tightly compacted (Fig.15).

Consequently, horizontal stress difference is a good indicator for the compaction degree (Fig.15) (Lai et al., 2019a). High values of horizontal stress difference will result in a high degree of compaction, and the intergranular pore spaces will be low, and the rocks are easily to be tightly compacted (Fig.15). Conversely, rocks associated with low horizontal stress difference will experience a low degree of compaction, and the intergranular pore spaces can be preserved (Fig.15). High quality reservoirs are commonly associated with the layers with low horizontal stress differences (Fig.15).

Natural fractures are also mainly associated with the layers where $\Delta\sigma$ is low (Fig.16) (Lai et al., 2019a). There are 6 numbers of fractures picked out by image logs in Layer A of

Fig.16, and the related $\Delta\sigma$ value is only 40-42 MPa. Additionally, the Layer C in Fig.16 also has 6 fractures, and the calculated $\Delta\sigma$ value is only 40 MPa. Conversely, the high $\Delta\sigma$ layers commonly relate to the non-fracture (tight matrix rock) intervals (Layer B in Fig.16).

5.2. Fracture and dissolution

Fractures are mainly encountered in fine-medium grained sandstones, while the conglomerates and mudstones have rare fractures (Fig.7). In addition, the dissolution pores are also commonly detected in the fine-medium grained sandstones, conversely, those very fine-grained rocks or pebby sandstones have low content of intergranular pores and consequently the dissolution pores are also rarely observed (Fig.5), since the presence of intergranular will be favorable for formation of dissolution pores.

Coupling observation of thin sections and image logs shows that fractures are easily to be dissolved along the fracture surfaces (Fig.17). In addition, microscopic observation of thin section reveals that dissolution pores are also commonly associated with the fractured layers (Fig.17). In some cases, the dissolution enlarged pores can be detected, indicating a high degree of dissolution. Decameter-scale porosity can even be formed in carbonate rocks due to the fracture-enhanced dissolution in carbonate rocks (Ukar et al., 2020). Additionally, microfractures are observed to be coexisted with the intergranular and intragranular dissolution pores (Fig.17). The presences of fractures enhance fluid flow, and will improve grain dissolution in sandstones (Fig.18). In fractured intervals, the thin section confirms the presence of intergranular and intragranular dissolution pores, and the dissolution pores are commonly coexisting with intergranular pores (Fig.17; Fig.18).

Dissolution pores are mainly associated with natural fractures, and vuggy fracture surfaces can be observed (Fig.19). Conversely no evident dissolution pores are observed in layer without fractures (Fig.19). Therefore the presences of natural fractures greatly improve fluid flow and will enhance framework grain dissolution, forming intergranular and intragranular dissolution pores.

5.3. Fracture-diagenesis within structure patterns

In foreland fold-and-thrust belts in Kuqa depression, the stress is concentrated (Ju and Wang, 2018; Feng et al., 2018), and large amounts of fractures are formed (Fig.20). However, the natural fractures show no evident relationships with burial depth as picked out by image logs, and they can form well connected fluid flow channels (Fig.20). The deep and shallow lateral logs (M2Rx, M2R3) show evident separation characteristics in fractured zones, which implies a favorable flow property (Fig.20). The structural position (anticline hinge vs limb) will affect the horizontal stress differences, and variations of compaction and fracturing will be encountered.

The Well Bozi 102, which was drilled in an anticline, also shows high density of natural fractures (Fig.21). However, there is also no increasing or decreasing trend of fracture density with burial depth. The fractured zones also show evident shallow and deep resistivity deviations, indicating a favorable fluid capacity (Fig.21). When combining thin section observation with image logs, it is found that the fractured zones enhance framework grain dissolution (Fig.21). The presences of intergranular and intragranular dissolution pores are mainly associated with the fractured zones (Fig.21). Additionally, the fracture surfaces can themselves be dissolved as interpreted from the image logs, and the dissolution pores will be formed since the fractures improve fluid flow and enhance grain dissolution (Fig.21). Conversely, the layers with no evident dissolution pores are mainly related to the non-fracture zones (Fig.21).

The Well KS 8, which was also drilled at the core part of an anticline, also shows high degree of fracture development (Fig.22). Also the fractures are not controlled by burial depth. In the vertical geophysical cross section, there is an overall increase of $\Delta\sigma$ with burial depths (Fig.22). The fractured zones are mainly associated with the low $\Delta\sigma$ layers, in addition, the rocks with evident intergranular pores also are characterized by low $\Delta\sigma$ values (Fig.22). Consequently, high quality reservoirs with intergranular pores or fractures are associated with the low $\Delta\sigma$ layers (Fig.22). The presences of intergranular pores have no evident relationships with fractures, and they can be elsewhere providing the $\Delta\sigma$ values are low (Fig.22). However, the layers with evident dissolution pores or microfractures are mainly corresponding with the fractured zones, and these fractured zones are also characterized by a low $\Delta\sigma$ value (Fig.22). Consequently, the in situ stress magnitude is related to the structure pattern, and low $\Delta\sigma$ values are favorable for the preservation of intergranular pores. The fractured zones will also result in a low $\Delta\sigma$ stress. Dissolution pores are controlled by the presences of fractures (Fig.22).

To conclude, there are complicated compaction, multiple fracturing, and cementation and dissolution along the fractured zones, and a comprehensive structural diagenesis analysis by integrating geological and continuous petrophysical well log data will provide insights into the distribution of intergranular pores, dissolution pores as well as fracture developments. The comprehensive structural diagenesis analysis helps better understand the structural and diagenetic processes, and reduces the uncertainty in reservoir quality prediction of ultra-deep sandstones.

6. Conclusions

Relationships between thrust faults and fault-related folds and diagenesis in Kuqa depress are investigated, and the following conclusions can be drawn:

The pore spaces in Lower Cretaceous Bashijiqike Formation consist of residual intergranular pores, intergranular and intragranular dissolution pores. The sandstones experienced a high degree of mechanical compaction, and the compaction is limited in well –sorted rocks or rocks abundant in rigid grains. The most volumetrically important diagenetic minerals are carbonates (in the form of calcites and dolomites). Dissolution degree is varied, and intergranular and intragranular pore spaces are formed.

Natural fracture attitude and status are characterized by image logs, and fracture parameters including fracture porosity, fracture density, fracture length and fracture aperture are calculated. Special aims are paid on the dissolution along the fracture planes. There are abundant natural fractures cemented by carbonate cements. No matter high angle, low angle or even horizontal fractures are highly cemented. Cementation along the fracture surfaces limits fluid flow. In addition, core and image log observation reveal that fracture enhances dissolution, and the fracture planes are enlarged by dissolution. The cementation and dissolution can occur simultaneously in a fracture surface in some cases, and the enlarged fracture surfaces can be fully cemented by late-stage cements.

The magnitudes of vertical stress Sv, maximum horizontal stress (SHmax), and minimum horizontal stress (Shmin) are calculated by constructing one-dimensional mechanical Earth models. The horizontal stress difference (Δσ) determines the compaction degree, and rocks associated with low horizontal stress difference experienced a low degree of compaction, and the intergranular pore spaces can be preserved. Additionally, natural fractures are also mainly associated with the low Δσ layers.

Dissolution pores are mainly associated with fractured zones since the presences of fractures enhance fluid flow. The presences of intergranular and intragranular dissolution pores are mainly associated with the fractured zones. The high quality reservoirs with intergranular pores or fractures are associated with low Δσ layers. Structural diagenesis which integrates diagenesis with fracture, in situ stress and structure patterns provides new insights into the reservoir quality evaluation of ultra-deep sandstones in Kuqa depression.

Acknowledgments

This work is financially supported by National Natural Science Foundation of China (No. 41872133), Natural Science Foundation of Beijing (8204069) and Science Foundation of China University of Petroleum, Beijing (No. 2462021YXZZ003). We thank the PetroChina Tarim Oilfield Company for their technical input.

Author Contribution Statement

Jin Lai, Dong Li and Guiwen Wang: Conceptualization, Methodology, Software

Yong Ai, Hongkun Liu and Deyang Cai: Data curation, Writing- Original draft preparation.

Kangjun Chen, Yuqiang Xie: Visualization, Investigation.

Dong Li, Guiwen Wang: Software, Validation.

Jin Lai, Guiwen Wang: Writing- Reviewing and Editing.

Competing interests

The authors declare that they have no known competing financial interests or personal relationships that could have appeared to influence the work reported in this paper.

Data availability

The data used to support the findings of this study are available from the corresponding author upon request.

References

Ameen M.S., and Hailwood E. A., 2008. A new technology for the characterization of microfractured reservoirs (test case: Unayzah reservoir, Wudayhi field, Saudi Arabia). AAPG Bulletin 92(1), 31–52.

Ameen, M. S., MacPherson K., Al-Marhoon M. I., and Rahim Z., 2012, Diverse fracture properties and their impact on performance in conventional and tight-gas reservoirs, Saudi Arabia: The Unayzah, South Haradh case study. AAPG Bulletin 96(3), 459–492.

Baqués, V., Ukar, E., Laubach, S.E., Forstner, S.R., Fall, A., 2020. Fracture, dissolution, and cementation events in Ordovician carbonate reservoirs, Tarim basin, NW China.

Geofluids, v. 2020, Article ID 9037429. doi: 10.1155/2020/9037429
Bell, J. S., Gough, D. I. 1979. Northeast-southwest compressive stress in Alberta: evidence from oil wells. Earth & Planetary Science Letters, 45(2), 475-482.
Bruna V.L., Lamarche J., Agosta F., Rustichelli A., Giuffrida A., Salardon R., Marié L.2020. Structural diagenesis of shallow platform carbonates: Role of early embrittlement on fracture setting and distribution, case study of Monte Alpi (Southern Apennines, Italy). Journal of Structural Geology 131, 103940.
Chen, J.F., Xu Y.C., Huang D.F., 2000. Geochemical Characteristics and Origin of Natural Gas in Tarim Basin, China : AAPG Bulletin, 84(5), 591–606.
Del Sole, L., Antonellini, M., Soliva, R., Ballas, G., Balsamo, F., and Viola, G.: Structural control on fluid flow and shallow diagenesis: insights from calcite cementation along deformation bands in porous sandstones, Solid Earth, 11, 2169–2195.
Dixit N.C., Hanks C.L., Wallace W.K., Ahmadi M., and Awoleke O. 2017. In situ stress variations associated with regional changes in tectonic setting, northeastern Brooks Range and eastern North Slope of Alaska. AAPG Bulletin, 101(3), 343–360.
Feng J., Ren Q., Xu K. 2018. Quantitative prediction of fracture distribution using geomechanical method within Kuqa Depression, Tarim Basin, NW China. Journal of Petroleum Science and Engineering 162, 22–34.
Ferraro F., Agosta F., Ukar E., Grieco D.S., Cavalcante F., Belviso C., Prosser G. 2019. Structural diagenesis of carbonate fault rocks exhumed from shallow crustal depths: An example from the central-southern Apennines, Italy. Journal of Structural Geology 122, 58–80.

Fu Q. 2019. Characterization and discrimination of paleokarst breccias and pseudobreccias in carbonate rocks: Insight from Ordovician strata in the northern Tarim Basin, China. Sedimentary Geology, 382, 61–74.

Gao Z., Liu Z., Gao S., Ding Q., Wu S., Liu S. 2016. Characteristics and genetic models of Lower Ordovician carbonate reservoirs in southwest Tarim Basin, NW China. Journal of Petroleum Science and Engineering, 144, 99–112.

Haile B.G., Klausen T.G. Czarniecka U., Xi K., Jahren J., Hellevang H. 2018. How are diagenesis and reservoir quality linked to depositional facies? A deltaic succession, Edgeøya, Svalbard. Marine and Petroleum Geology 92, 519–546.

Hassani, A.H., Veyskarami, M., Al-Ajmi, A.M., Masihi, M., 2017. A modified method for predicting the stresses around producing boreholes in an isotropic in-situ stress field. Int. J. Rock Mech. Min. Sci. 96, 85–93.

Houseknecht, D.W., 1987, Assessing the relative importance of compaction processes and cementation to reduction of porosity in sandstones: American Association of Petroleum Geologists, Bulletin, v. 71, p. 633–642.

Higgs, K.E., Zwingmann, H., Reyes, A.G., and Funnell, R.H., 2007. Diagenesis, porosity evolution, and petroleum emplacement in tight gas reservoirs, Taranaki basin, New Zealand: Journal of Sedimentary Research, v.77, p.1003–1025.

Iqbal O., Ahmad M., Kadir A. 2018. Effective evaluation of shale gas reservoirs by means of an integrated approach to petrophysics and geomechanics for the optimization of hydraulic fracturing: A case study of the Permian Roseneath and Murteree Shale Gas reservoirs, Cooper Basin, Australia. Journal of Natural Gas Science and Engineering 58,

34–58.
Jiang L., Cai C., Worden R.H., Crowley S.F., Jia L., Zhang K., and Duncan I.J. 2016. Multiphase dolomitization of deeply buried Cambrian petroleum reservoirs, Tarim Basin, north-west China. Sedimentology, 63, 2130–2157.
Jia, C. Z., Li, Q., 2008. Petroleum geology of Kela–2, the most productive gas field in China. Marine and Petroleum Geology 25, 335–343.
Ju, W., Hou, G., Zhang, B., 2014. Insights into the damage zones in fault–bend folds from geomechanical models and field data. Tectonophysics 610, 182–194.
Ju, W., Shen, J., Qin, Y., Meng, S., Wu, C., Shen, Y., Yang Z., Li G., Li C. 2017. In-situ stress state in the Linxing region, eastern Ordos basin, china: implications for unconventional gas exploration and production. Marine and Petroleum Geology, 86, 66-78.
Ju W., Wang K. 2018. A preliminary study of the present-day in-situ stress state in the Ahe tight gas reservoir, Dibei Gasfield, Kuqa Depression. Marine and Petroleum Geology 96, 154–165.
Ju Wei, Shen Jian, Li Chao, Yu Kun, Yang Hui. 2020. Natural fractures within unconventional reservoirs of Linxing Block, eastern Ordos Basin, central China. Frontier of Earth Science, 14(4): 770–782.
Jin, Z.J., Yang M.H., Lu X.X., Sun D.S., Tang X., Peng G.X., Lei G.L., 2008. The tectonics and petroleum system of the Qiulitagh fold and thrust belt, northern Tarim basin, NW China: Marine and Petroleum Geology, 25, 767–777.
Kamp P.C. 2019. Provenance, shallow to deep diagenesis, and chemical mass balance in

supermature arenites and pelites, Ordovician Simpson Group, Oklahoma and Kansas, U.S.A. Sedimentary Geology 386, 79–102.

Keeton G.., Pranter M.., Cole R. D., and Gustason E.R., 2015. Stratigraphic architecture of fluvial deposits from borehole images, spectral-gamma-ray response, and outcrop analogs, Piceance Basin, Colorado. AAPG Bulletin 99(10), 1929–1956.

Khoshbakht F., Memarian H., Mohammadnia M. 2009. Comparison of Asmari, Pabdeh and Gurpi formation's fractures, derived from image log. Journal of Petroleum Science and Engineering 67, 65–74.

Khoshbakht F., Azizzadeh M., Memarian H., Nourozi G.H., Moallemi S.A., 2012. Comparison of electrical image log with core in a fractured carbonate reservoir. Journal of Petroleum Science and Engineering 86–87, 289–296.

Lai J., Wang G. 2015. Fractal analysis of tight gas sandstones using High-Pressure Mercury Intrusion techniques. Journal of Natural Gas Science and Engineering, 24, 185–196.

Lai J., Wang G., Chai Y., Ran Y., Zhang X. 2015. Depositional and diagenetic controls on reservoir pore structure of tight gas sandstones: Evidence from Lower Cretaceous Bashijiqike Formation in Kelasu Thrust Belts, Kuqa Depression in Tarim Basin of West China. Resource Geology, 65(2):55–75.

Lai J., Wang G., Chai Y., Xin Y., Wu Q., Zhang X., and Sun Y. 2017a. Deep burial diagenesis and reservoir quality evolution of high-temperature, high-pressure sandstones: Examples from Lower Cretaceous Bashijiqike Formation in Keshen area, Kuqa depression, Tarim basin of China. AAPG Bulletin, 101(6): 829–862.

Lai, J., Wang G., Fan Z., Wang Z., Chen J., Zhou Z., Wang S., Xiao C. 2017b. Fracture detection in oil-based drilling mud using a combination of borehole image and sonic logs. Marine and Petroleum Geology, 84, 195–214.

Lai J., Wang G., Wang S., Cao J., Li M., Pang X., Han C., Fan X., Yang L., He Z., Qin, Z. 2018. A review on the applications of image logs in structural analysis and sedimentary characterization. Marine and Petroleum Geology, 95, 139–166.

Lai J., Li D., Wang G., Xiao C., Hao X., Luo Q., Lai L., Qin Z. 2019a. Earth stress and reservoir quality evaluation in high and steep structure: The Lower Cretaceous in the Kuqa Depression, Tarim Basin, China. Marine and Petroleum Geology, 101, 43–54.

Lai J., Li D., Wang G., Xiao C., Cao J., Wu C., Han C., Zhao X., Qin Z. 2019b. Can carbonate cementation be inhibited in continental red bed sandstone?. Journal of Petroleum Science and Engineering, 179, 1123-1135.

Lai J., Wang S., Zhang C., Wang G., Song Q., Chen X., Yang K., Yuan C. 2020. Spectrum of pore types and networks in the deep Cambrian to Lower Ordovician dolostones in Tarim Basin, China. Marine and Petroleum Geology, 112, 104081.

Lai J., Liu S., Xin Y., Wang S., Xiao C., Song Q., Chen X., Wang G., Qin Z, Ding X. 2021a. Geological-petrophysical insights in the deep Cambrian dolostone reservoirs in Tarim Basin, China. AAPG Bulletin, 105(11): 2263-2296.

Lai J., Chen K., Xin Y., Wu X., Chen X., Yang K., Song Q, Wang G, Ding X. 2021b. Fracture characterization and detection in the deep Cambrian dolostones in the Tarim Basin, China: Insights from borehole image and sonic logs. Journal of Petroleum Science and Engineering 196, 107659.

Laubach S.E., 2003. Practical approaches to identifying sealed and open fractures. AAPG

Bulletin 87(4), 561–579.

Laubach, S.E., Olson, J.E., Gale, J.F.W., 2004. Are open fractures necessarily aligned with maximum horizontal stress? Earth and Planetary Science Letters 222, 191–195.

Laubach, S.E., Eichhubl, P., Hilgers, C., Lander, R.H. 2010. Structural diagenesis. Journal of Structural Geology, 32, 1866–1872.

Laubach S.E., Lamarche J., Gauthier B.D.M. Dunne, W.M., Sanderson D.J. 2018. Spatial arrangement of faults and opening-mode fractures. Journal of Structural Geology 108, 2-15.

Laubach, S.E., Lander, R.H., Criscenti, L.J., Anovitz L. M., Urai J. L., Pollyea R. M., Hooker J. N., Narr W., Evans M. A., Kerisit S. N., Olson J. E., Dewers T., Fisher D., Bodnar R., Evans B., Dove P., Bonnell L. M., Marder M. P., and Pyrak-Nolte L., 2019. The role of chemistry in fracture pattern development and opportunities to advance interpretations of geological materials. Review of Geophysics 57 (3), 1065–1111.

Lyu, W., Zeng, L., Liu, Z., Liu, G., Zu, K., 2016. Fracture responses of conventional logs in tight-oil sandstones: a case study of the Upper Triassic Yanchang Formation in southwest Ordos Basin, China. AAPG Bulletin 100 (9), 1399–1417.

Lyu, W., Zeng, L., Zhang, B., Miao, F., Lyu, P., Dong, S. 2017. Influence of natural fractures on gas accumulation in the Upper Triassic tight gas sandstones in the northwestern Sichuan Basin, China. Marine and Petroleum Geology 83, 60–72.

Lima, R.D., and DeRos, L.F., 2002. The role of depositional setting and diagenesis on the reservoir quality of Devonian sandstones from the Solimo˜es Basin, Brazilian Amazonia: Marine and Petroleum Geology, v.19, p.1047–1071.

Mansurbeg, H., Morad, S., Salem, A., Marfil, R., El–ghali, M.A.K., Nystuen, J.P., Caja, M.A., Amorosi, A., Garcia, G., and Iglesia, A.L., 2008. Diagenesis and reservoir quality evolution of palaeocene deep–water, marine sandstones, the Shetland–Faroes Basin, British continental shelf: Marine and Petroleum Geology, v.25, p.514–543.

Massiot, C., Mcnamara, D. D., Lewis, B. 2015. Processing and analysis of high temperature geothermal acoustic borehole image logs in the Taupo volcanic zone, New Zealand. Geothermics, 53, 190-201.

Maleki, S., Moradzadeh, A., Riabi, R. G., Sadaghzadeh, F. 2014. Comparison of several different methods of in situ stress determination. International Journal of Rock Mechanics & Mining Sciences, 71(71), 395-404.

Matonti C., Lamarche J., Guglielmi Y., Marié L. 2012. Structural and petrophysical characterization of mixed conduit/seal fault zones in carbonates: Example from the Castellas fault (SE France). Journal of Structural Geology 39, 103-121.

Matonti C., Guglielmi Y., Viseur S., Garambois S., Marié L. 2017. P-wave velocity anisotropy related to sealed fractures reactivation tracing the structural diagenesis in carbonates. Tectonophysics 705, 80–92.

Neng Y., Xie H., Yin H., Li Y., Wang W. 2018. Effect of basement structure and salt tectonics on deformation styles along strike: An example from the Kuqa fold–thrust belt, West China. Tectonophysics 730, 114-131.

Nian, T., Wang, G., Xiao, C., Zhou, L., Deng, L., Li, R. 2016. The in situ stress determination from borehole image logs in the Kuqa Depression. Journal of Natural Gas Science and Engineering, 34, 1077-1084.

Nian, T., Wang, G., Song, H. 2017. Open tensile fractures at depth in anticlines: a case study in the Tarim basin, NW China. Terra Nova, 29(3),183-190.

Nian T., Jiang Z., Wang G., Xiao C., He W., Fei L., He Z. 2018. Characterization of braided river-delta facies in the Tarim Basin Lower Cretaceous: Application of borehole image logs with comparative outcrops and cores. Marine and Petroleum Geology 97, 1–23.

Nian T., Wang G., Tan C., Fei L., He W., Wang S. 2021. Hydraulic apertures of barren fractures in tight-gas sandstones at depth: Image-core calibration in the lower cretaceous Bashijiqike Formation, Tarim Basin. Journal of Petroleum Science and Engineering 196, 108016.

Nie X. Zou C., Pan L., Huang Z., Liu D., 2013. Fracture analysis and determination of in-situ stress direction from resistivity and acoustic image logs and core data in the Wenchuan Earthquake Fault Scientific Drilling Borehole-2 (50–1370 m). Tectonophysics 593, 161–171.

Nelson, R.A., 2001. Geologic Analysis of Naturally Fractured Reservoirs, second ed. Gulf Professional Publishing, Woburn, Massachusetts, p. 332.

Ozkan, A., Cumella, S P., Milliken, K L., and Laubach, S.E., 2011. Prediction of lithofacies and reservoir quality using well logs, Late Cretaceous Williams Fork Formation, Mamm Creek field, Piceance Basin, Colorado: AAPG Bulletin, v.95, no.10, p.1699–1723.

Qiu, N.S., Chang J., Zuo Y.H., Wang J.Y, Li H.L., 2012. Thermal evolution and maturation of lower Paleozoic source rocks in the Tarim Basin, northwest China: AAPG Bulletin, v. 96, no. 5, p. 789–821.

Rodrigues R.S., Alves da Silva F. C., Córdoba V.C. 2021. Evolution of deformation bands, insights from structural diagenesis. Journal of Structural Geology 143, 104257.

Schultz C.D., Hofmann M.H. 2021. Facies, stratigraphic architecture, and faults - The controls on the cement distribution in the Devonian Sappington Formation in southwestern Montana. Marine and Petroleum Geology 124, 104806.

Shen, Y., Lü, X., Guo, S., Song, X., Zhao, J. 2017. Effective evaluation of gas migration in deep and ultra-deep tight sandstone reservoirs of Keshen structural belt, Kuqa depression. Journal of Natural Gas Science and Engineering, 46, 119-131.

Tingay, M.R.P., Hillis, R.R., Morley, C.K., King, R.C., Swarbrick, R.E., Damit, A.R., 2009. Present-day stress and neotectonics of Brunei: implications for petroleum exploration and production. AAPG Bull. 93, 75-100.

Ukar, E. and Laubach, S.E., 2016. Syn- and postkinematic cement textures in fractured carbonate rocks: Insights from advanced cathodoluminescence imaging, Tectonophysics 690, Part A, 190-205, doi: 10.1016/j.tecto.2016.05.001

Ukar, E., Baqués, V., Laubach, S.E., Marrett, R., 2020. The nature and origins of decameter-scale porosity in Ordovician carbonate rocks, Halahatang oilfield, Tarim Basin, China. Journal of the Geological Society, 177, 1074-1091. doi:10.1144/jgs2019-156

Vandeginste V., Swennen R., Allaeys M., Ellam R.M., Osadetz K., Roure F. Challenges of structural diagenesis in foreland fold-and-thrust belts: A case study on paleofluid flow in the Canadian Rocky Mountains West of Calgary. Marine and Petroleum Geology 35, 235-251.

Verweij J.M., Boxem T.A.P., Nelskamp S. 2016. 3D spatial variation in vertical stress in on- and offshore Netherlands; integration of density log measurements and basin modeling results. Marine and Petroleum Geology, 78, 870-882.

Wang, J., Wang, H., Chen, H., Jiang, S. and Zhao, S., 2013. Responses of two lithosomes of Lower Cretaceous coarse clastic rocks to tectonism in Kuqa foreland sub–basin, Northern Tarim Basin, Northwest China. Sedimentary Geology 289, 182–193.

Wang, J., Zeng, L., Yang, X., Liu, C., Wang, K., Zhang, R., Chen, X., Qu, Y., Laubach, S.E., Wang, Q, 2021. Fold-related fracture distribution in Neogene, Triassic, and Jurassic sandstone outcrops, northern margin of the Tarim Basin, China: Guides to deformation in ultradeep tight sandstone reservoirs. Lithosphere, 8330561. https://doi.org/10.2113/2021/8330561

Wei Guoqi, Wang Junpeng, Zeng Lianbo, Tang Yongliang, Wang Ke, Liu Tiantian, Yang Yu. Structural reworking effects and new exploration discoveries of subsalt ultra-deep reservoirs in the Kelasu tectonic zone. Natural Gas Industry, 2020, 40(1): 20-30.

Wilson, T. H., Smith, V., Brown, A. 2015. Developing a model discrete fracture network, drilling, and enhanced oil recovery strategy in an unconventional naturally fractured reservoir using integrated field, image log, and three-dimensional seismic data. AAPG Bulletin, 99(4), 735-762.

Wu Guanghui, Xie En, Zhang Yunfeng, Qing Hairuo, Luo Xinsheng and Sun Chong. 2019. Structural diagenesis in carbonate rocks as identified in fault damage zones in the Northern Tarim Basin, NW China. Minerals, 9, 360.

Yeltsov, I. N., Nazarova, L. A., Nazarov, L. A., Nesterova, G. V., Sobolev, A. Y., & Epov, M.

I. 2014. Geomechanics and fluid flow effects on electric well logs: multiphysics modeling. Russian Geology and Geophysics, 55(5–6), 775-783.

Zoback, M., Barton, C., Brudy, M., Castillo, D., Finkbeiner, T., Grollimund, B., Moos, D., Peska, P., Ward,C., Wiprut, D., 2003. Determination of stress orientation and magnitude in deep wells. International Journal of Rock Mechanics and Mining Sciences 40, 1049–1076.

Zhang, Y., Zhang, J. 2017. Lithology-dependent minimum horizontal stress and in-situ stress estimate. Tectonophysics, 703–704, 1-8.

Zhang, J., Qin L., Zhang Z., 2008. Depositional facies, diagenesis and their impact on the reservoir quality of Silurian sandstones from Tazhong area in central Tarim Basin, western China: Journal of Asian Earth Sciences v.33, p.42–60.

Zhang Hui, Yin Guoqing, Wang Zhimin, Wang Haiying. Fracability Evaluation of Deep-Burial Fractured Sandstone Gas Reservoir in Kuqa Depression. Xinjiang Petroleum Geology, 2019, 40(1): 108-115.

Zhang Jincai. 2011. Pore pressure prediction from well logs: Methods, modifications, and new approaches. Earth-Science Reviews, 108 (1–2), 50-63.

Zhao, W.Z., Zhang S.C., Wang F.Y., Cramer B., Chen J.P., Sun Y.G., Zhang B.M., Zhao M.J. 2005. Gas systems in the Kuche Depression of the Tarim Basin: Source rock distributions, generation kinetics and gas accumulation history: Organic Geochemistry, v.36, p.1583–1601.

Zazoun R S., 2013. Fracture density estimation from core and conventional well logs data using artificial neural networks: The Cambro-Ordovician reservoir of Mesdar oil field, Algeria. Journal of African Earth Sciences 83, 55–73.

Zeng L.B., and Li X.Y., 2009. Fractures in sandstone reservoirs with ultra-low permeability: A case study of the Upper Triassic Yanchang Formation in the Ordos Basin, China. AAPG Bulletin 93(4), 461–477.

Zeng L., 2010. Microfracturing in the Upper Triassic Sichuan Basin tight-gas sandstones: Tectonic, overpressure, and diagenetic origins. AAPG Bulletin 94(12), 1811–1825.

Zeng, L.B., Wang H.J., Gong L., Liu B.M. 2010. Impacts of the tectonic stress field on natural gas migration and accumulation: A case study of the Kuqa Depression in the Tarim Basin, China: Marine and Petroleum Geology, v.27, p. 1616-1627.

Zeng Q., Mo T., Zhao J., Tang Y., Zhang R., Xia J., Hu C., Shi L. 2020. Characteristics, genetic mechanism and oil & gas exploration significance of high-quality sandstone reservoirs deeper than 7 000 m: A case study of the Bashijiqike Formation of Lower Cretaceous in the Kuqa Depression. Natural Gas Industry, 40(1): 38-47.

Zou Y., Zhao C., Wang Y., Zhao W., Peng P. Shuai Y., 2006. Characteristics and origin of natural gases in the Kuqa depression of Tarim basin, NW China. Organic Geochemistry 37, 280–290.

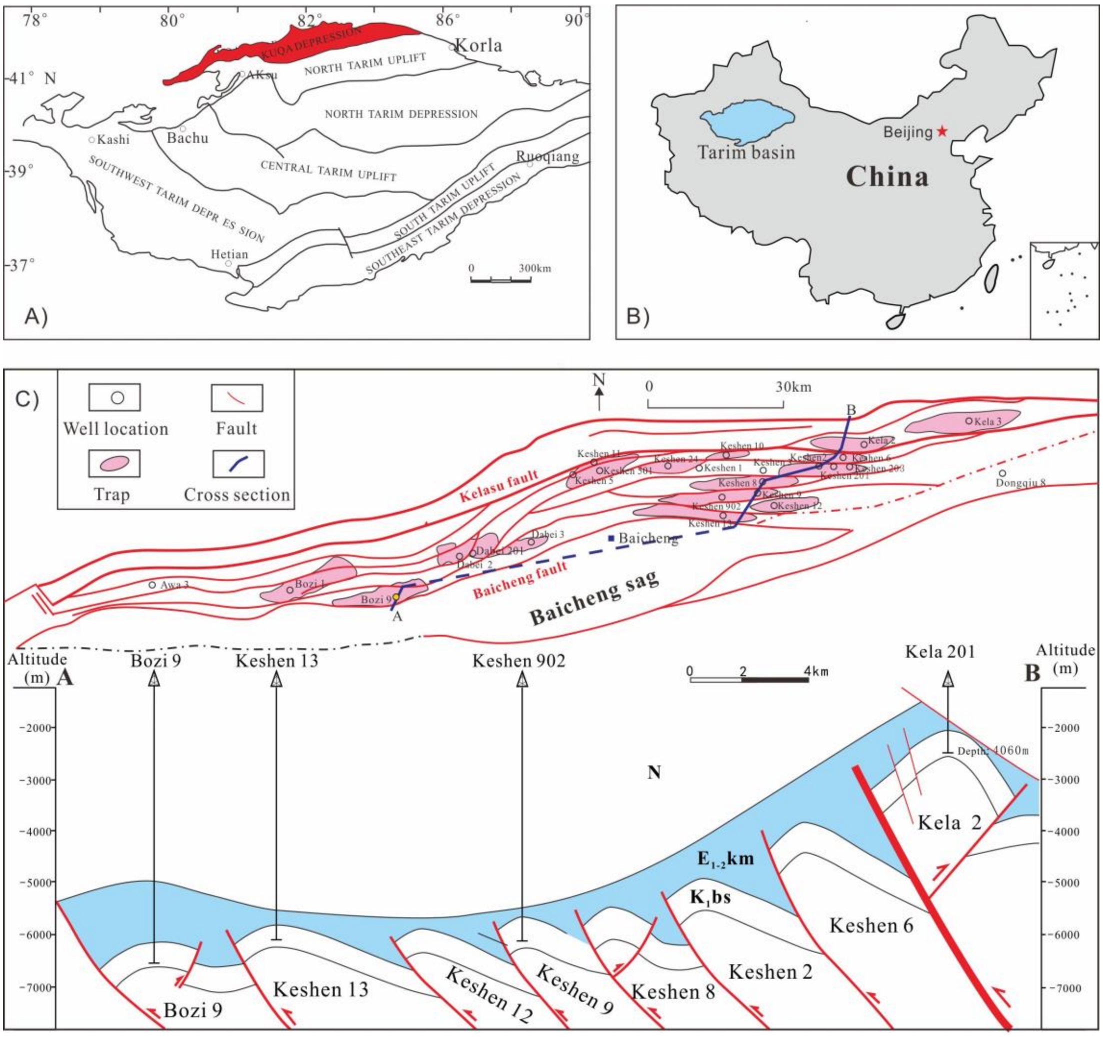

Figure 1. Map showing the structural divisions in the Kuqa Depression (C) within North Tarim basin (A), West China (B) (Jin et al., 2008; Lai et al., 2014; Lai et al., 2017; Wei et al., 2020)

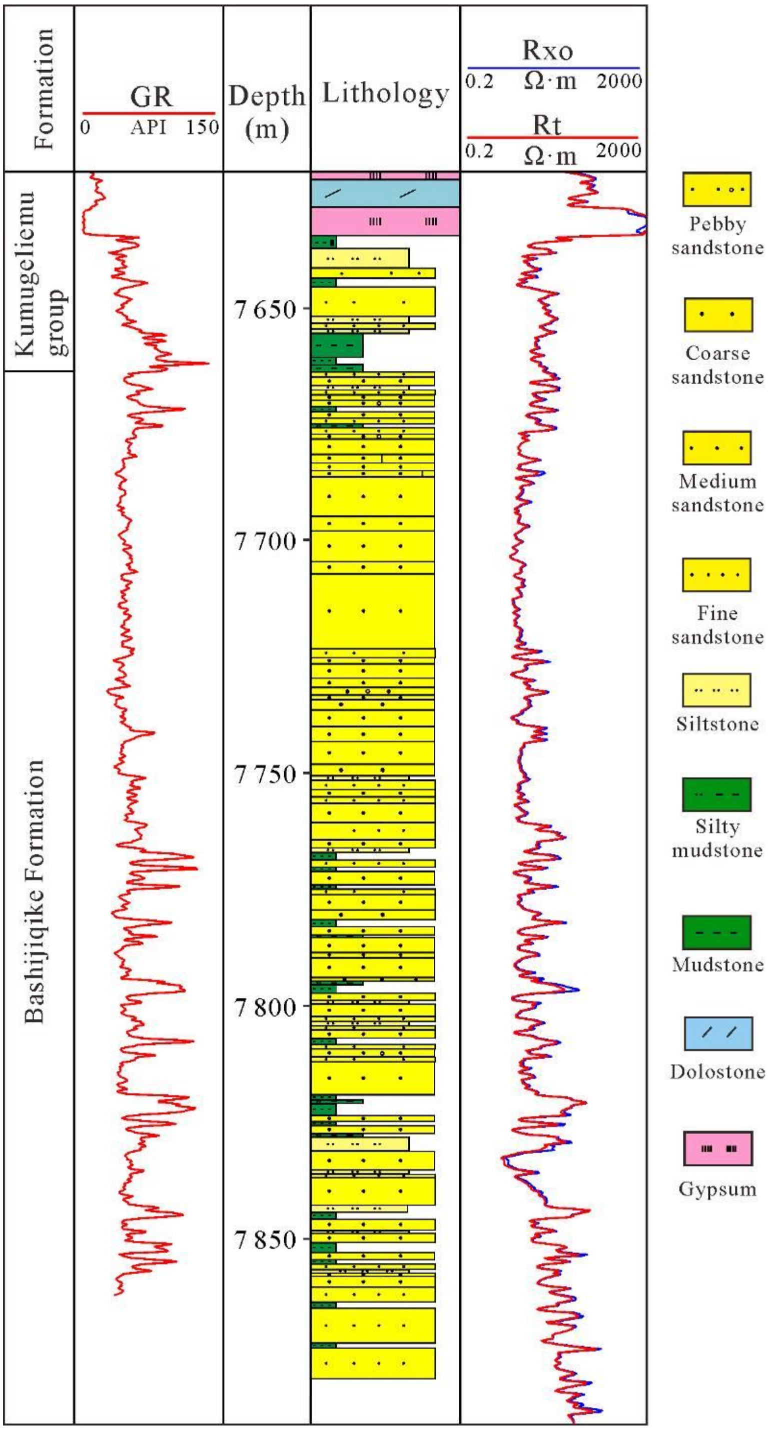

Figure 2. The lithology section and well log curves of Well Bozi 9 in Kuqa depression (Zeng et al., 2020)

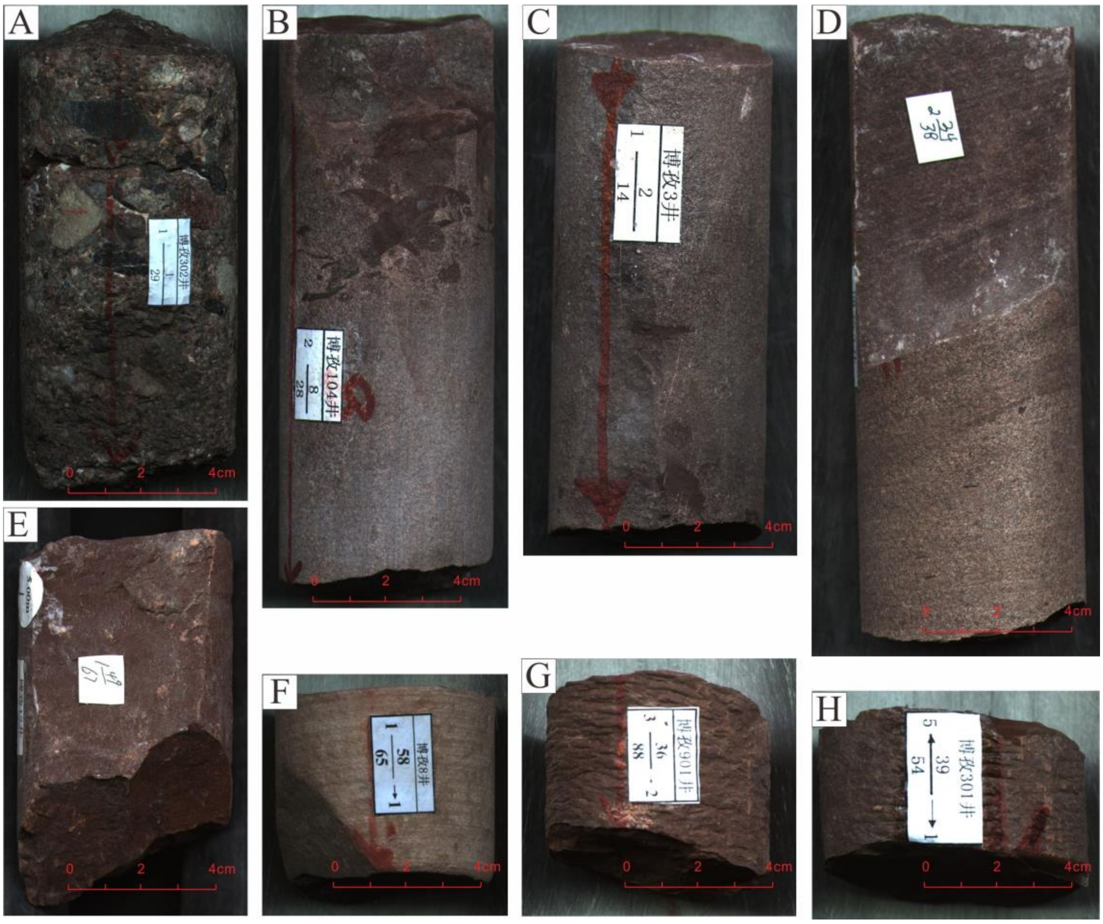

Figure 3. Core photos showing the lithologies of Cretaceous Bashijiqike Formation in Kuqa Depression

A. Conglomerates, Bozi 302

B. Pebby sandstones, Bozi 104

C. Medium-grained sandstone, Bozi 3

D. Fine-grained sandstones, Bozi 3

E. Siltstones, Bozi 12

F. Siltstones, Bozi 8

G. Mudstones, Bozi 901

H. Mudstones, Bozi 301

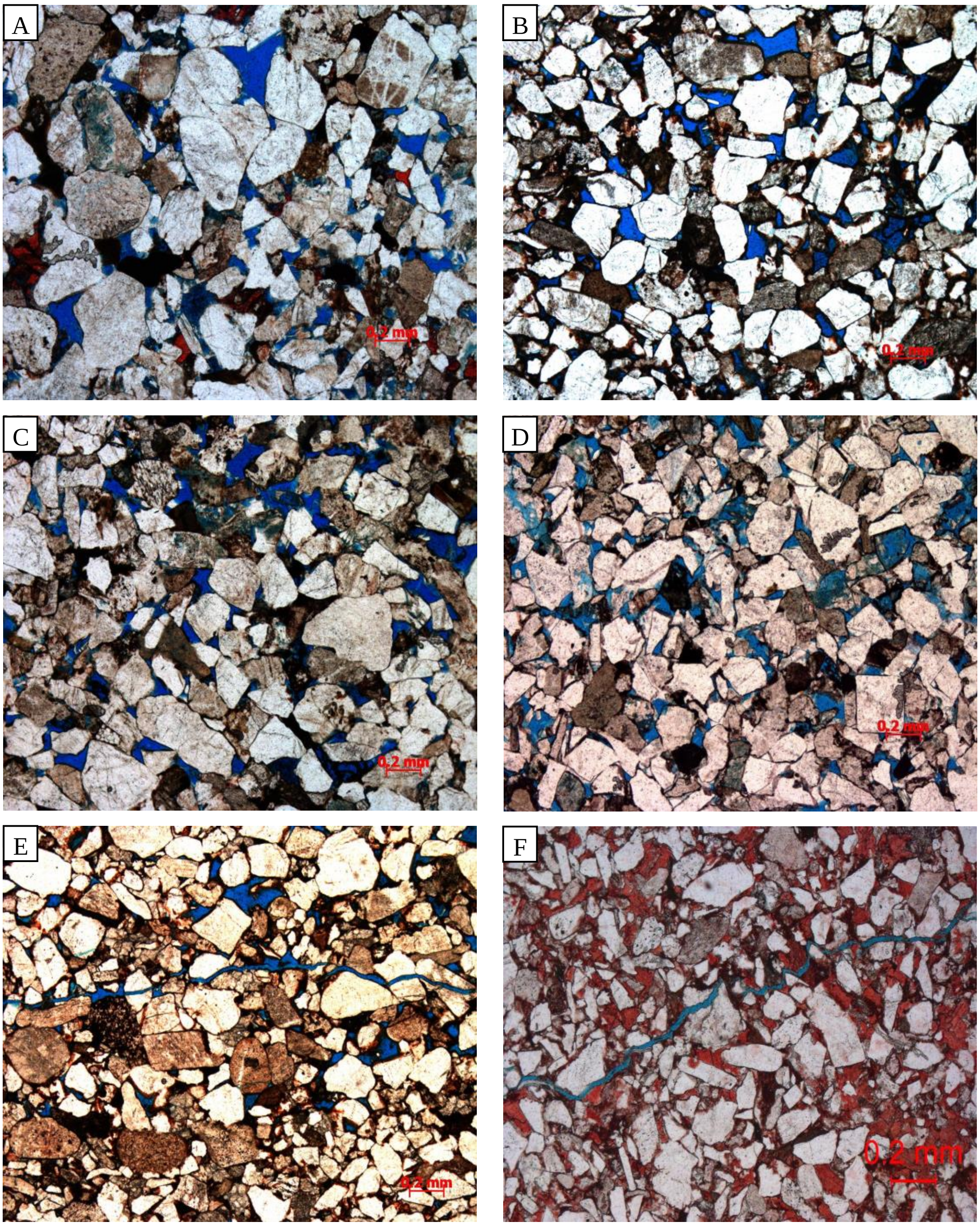

Figure 4. Thin section images showing the pore spaces of Cretaceous Bashijiqike Formation in Kuqa Depression

A. Intergranular pores, Bozi 301, 5843.8 m

B. Residual intergranular pores with irregular morphology, Bozi 9, 7689.32 m

C. Framework grain dissolved pores, Bozi 301, 5846.95 m

D. Intragranular dissolution pores, Keshen 242, 6564.1 m

E. Micro-fractures in sandstone with intergranular pore spaces, Bozi 9, 7675.95 m

F. Micro-fractures in carbonate cemented sandstone, Bozi 22, 6276.85m

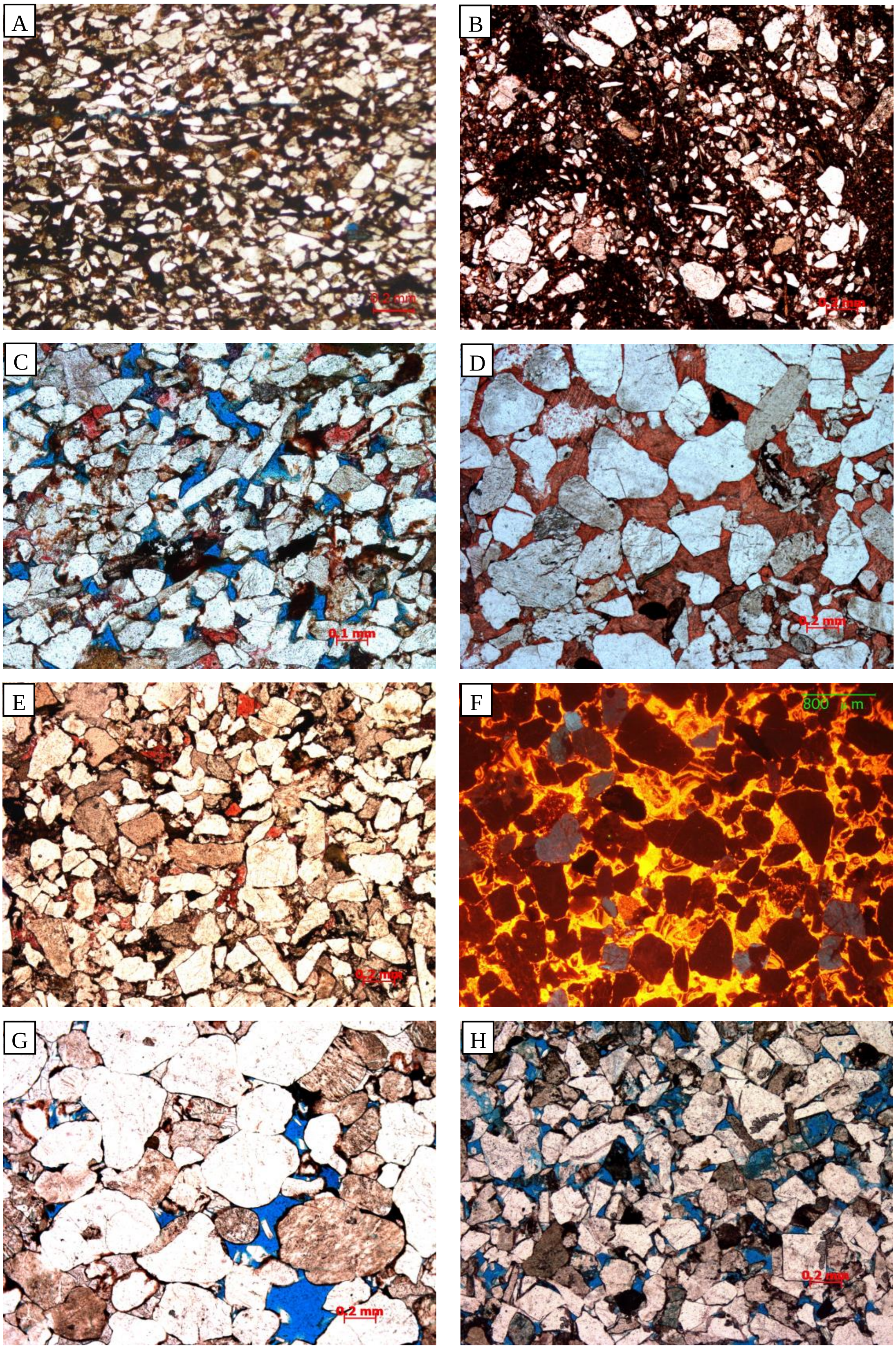

1
2
3
4

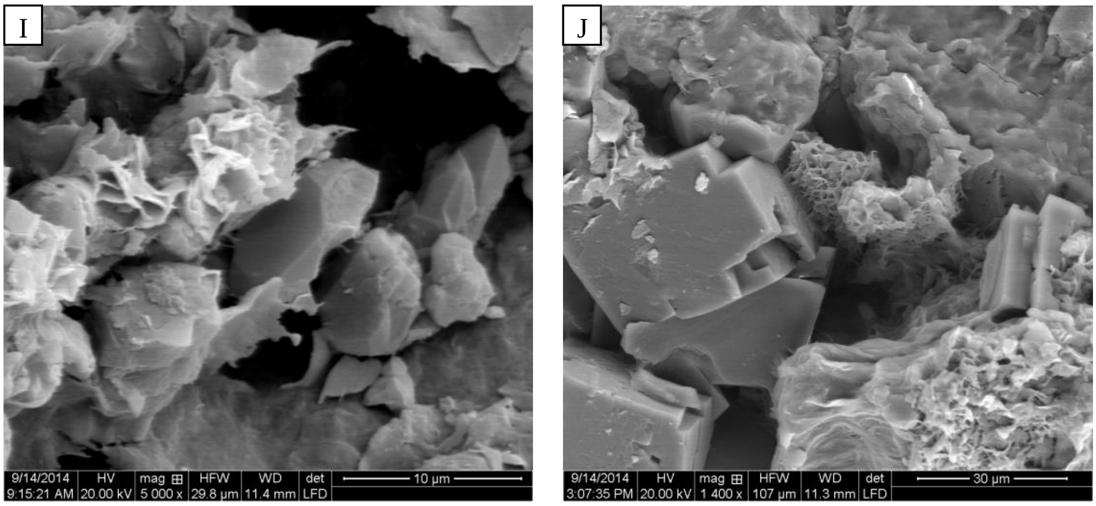

Figure 5. Thin section, CL and SEM images showing the diagenesis type and degree as well as diagenetic minerals of Cretaceous Bashijiqike Formation in Kuqa Depression

A. Tightly compacted rocks, very fine-grained, Dabei 902, 5097.15m

B. Poorly sorted rocks which are tightly compacted, Dabei 1102, 5921.26m

C. Intergraular pores preserved in well sorted rocks, Dabei 14, 6351.16 m

D. Extensive carbonate cements, Dabei 1101, 5895.76m

E. Dolomite cements, Dabei 1101, 5809.35m

F. CL images showing the extensive carbonate cements, Dabei 12, 5442.09 m

G. Dissolution pores due to dissolution of framework grains, Dabei 1102, 5915.51m

H. Intergranular and intragranular dissolution pores, Keshen 242, 6564.1m

I. Authigenic quartz and illite and smectite mixed layer, Bozi 102, 6758.04m

J. Illite and smectite mixed layer filling in the pore spaces, Bozi 102, 6763.16m

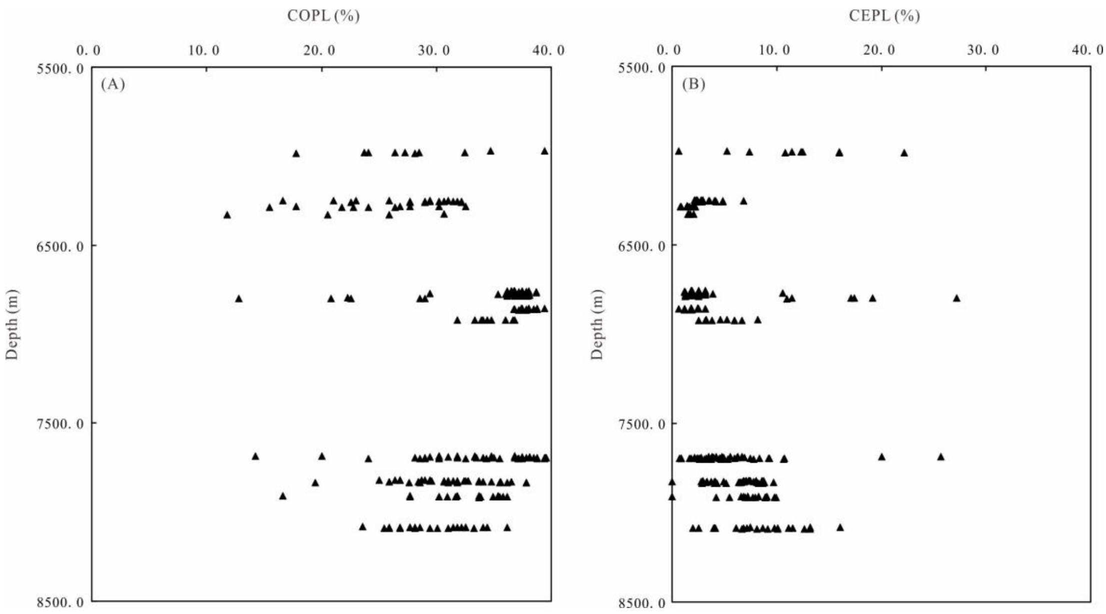

Figure 6. Plot of compactional porosity loss (COPL) and cementational porosity loss (CEPL) versus depth for the Bashijiqike sandstones

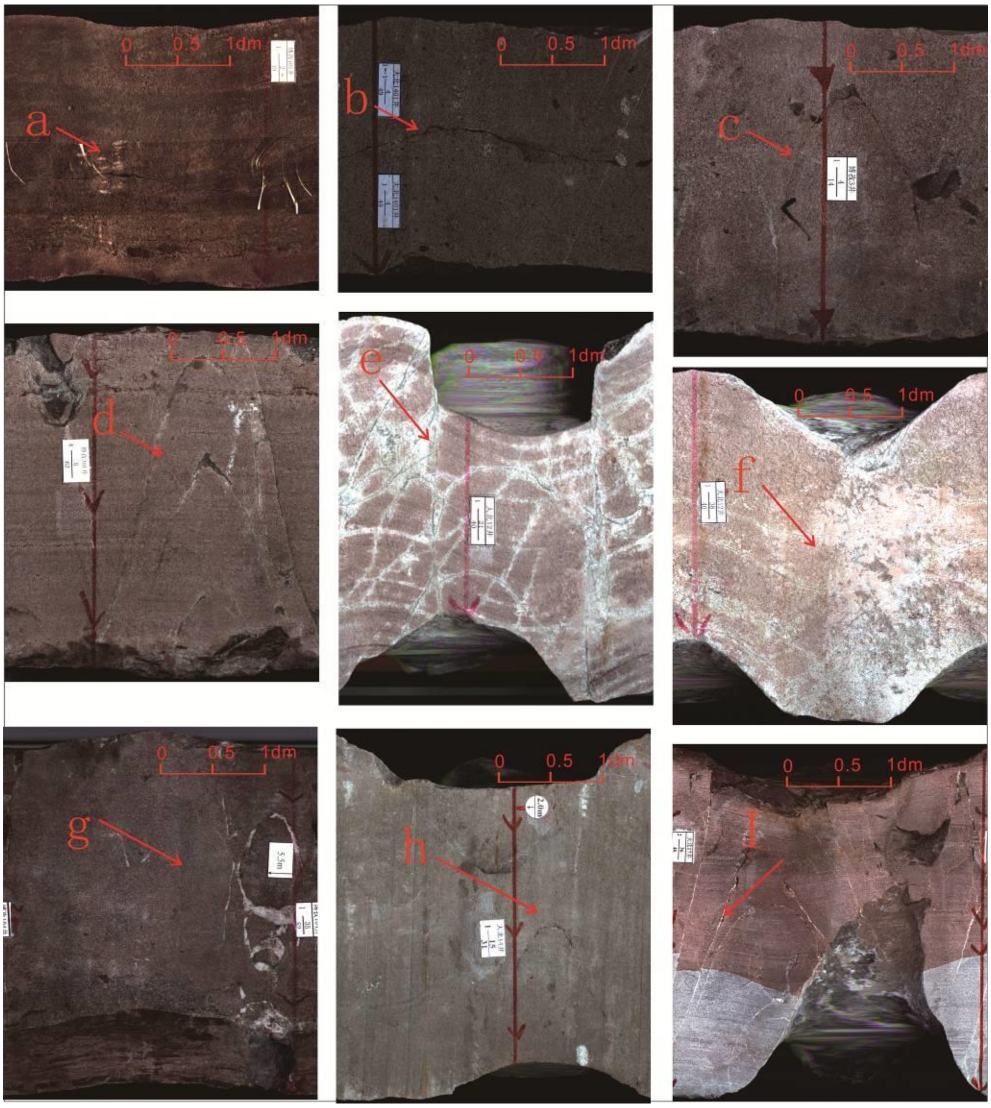

Figure 7. Core photos showing the various attributes and status of fracture

a. Horizontal fracture, fine-grained sandstones, Bozi 101, 6916.5m

b. Low angle fracture, fine-grained sandstones, Dabei 1401, 6351.4m

c. High angle fracture, fine-grained sandstones, Bozi 3, 5972m

d. Multi-set high angle fracture, medium-grained sandstones, Bozi 301, 5854.2m

e. Network fractures, medium-grained sandstones, Dabei 12, 5399.9m

f. Low angle fracture, medium-grained sandstones, Dabei 12, 5403.7m

g. Calcite-fillig high angle fracture, fine-grained sandstones, Bozi 104, 6803m

h. Fracture-enhanced dissolution, Dabei 14, 6349.6m

i. calcite filling and dossolution along the fracture planes, Dabei 17, 6154.2m

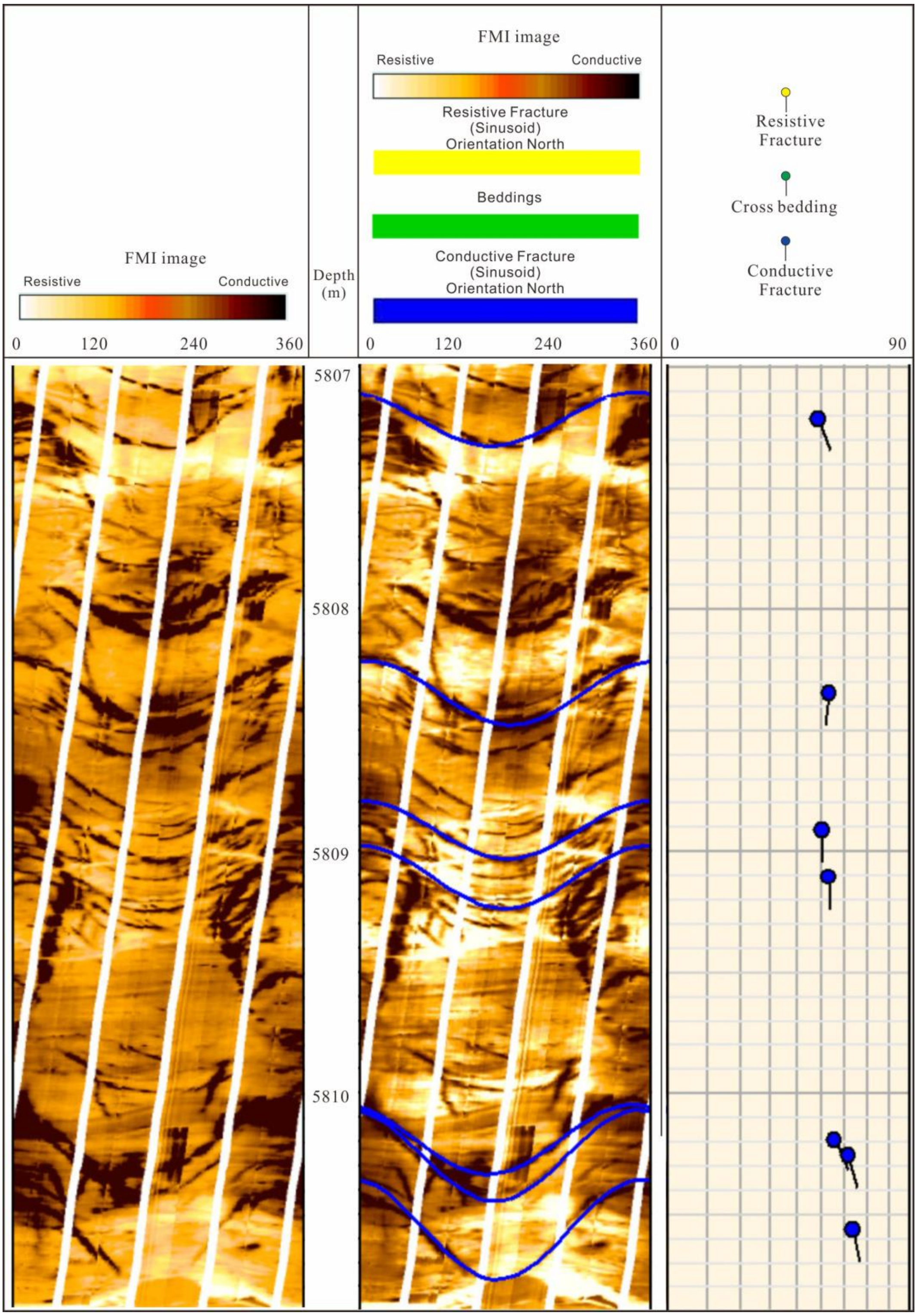

Figure 8. Fractures on the image logs picked out as dark sinusoidal waves

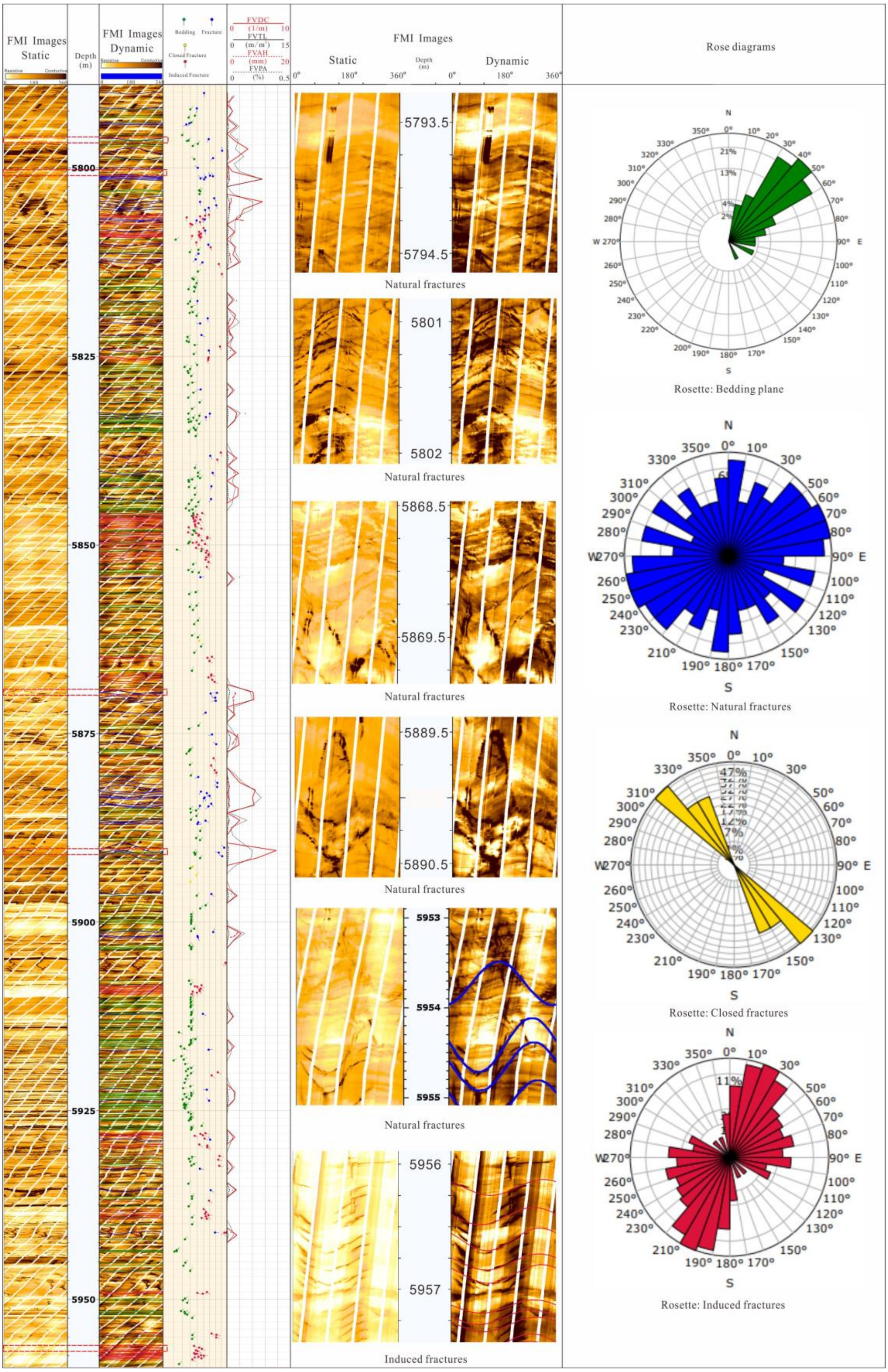

Figure 9. Comprehensive evaluation of natural fractures, induced fractures and fracture effectiveness using image logs for Dabei 1101

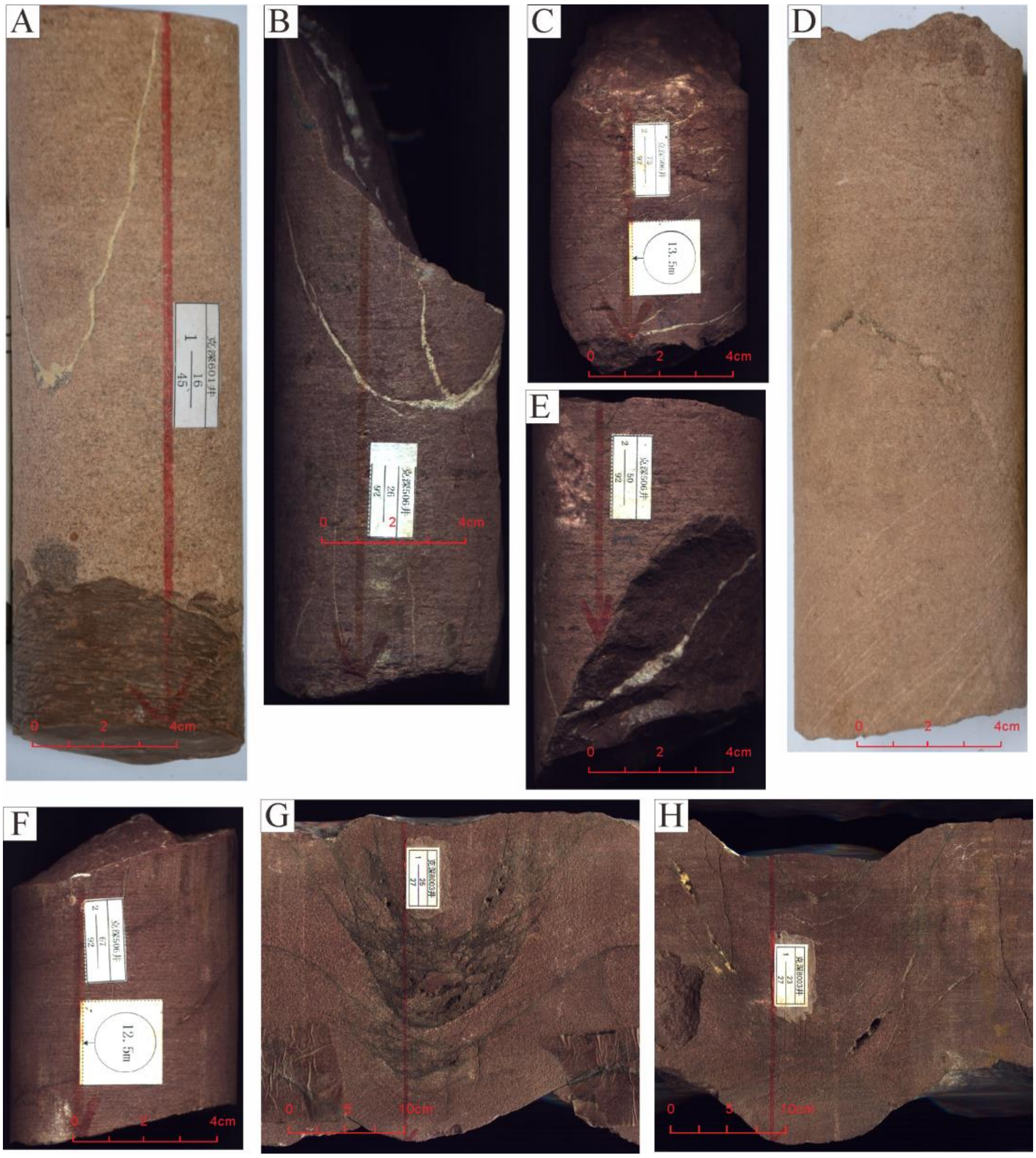

Figure 10. Core photos showing the cementation and dissolution along the fracture surfaces of Cretaceous Bashijiqike Formation in Kuqa Depression

A. Calcite cemented fracture planes (high angle), Keshen 601

B. Two calcite veins (high angle), Keshen 506

C. Horizontal fractures filled by calcite cements, Keshen 506

D. Dissolution along the fracture plane, enlarged fracture surfaces, Keshen 601, 2-31/57

E. Large calcite veins, Keshen 506

F. Mudstone filling in the fracture planes, Keshen 506

G. Dissolution along the fracture surfaces, forming vugs, Keshen 8003

H. Cementation and dissolution along the fracture surfaces, Keshen 8003

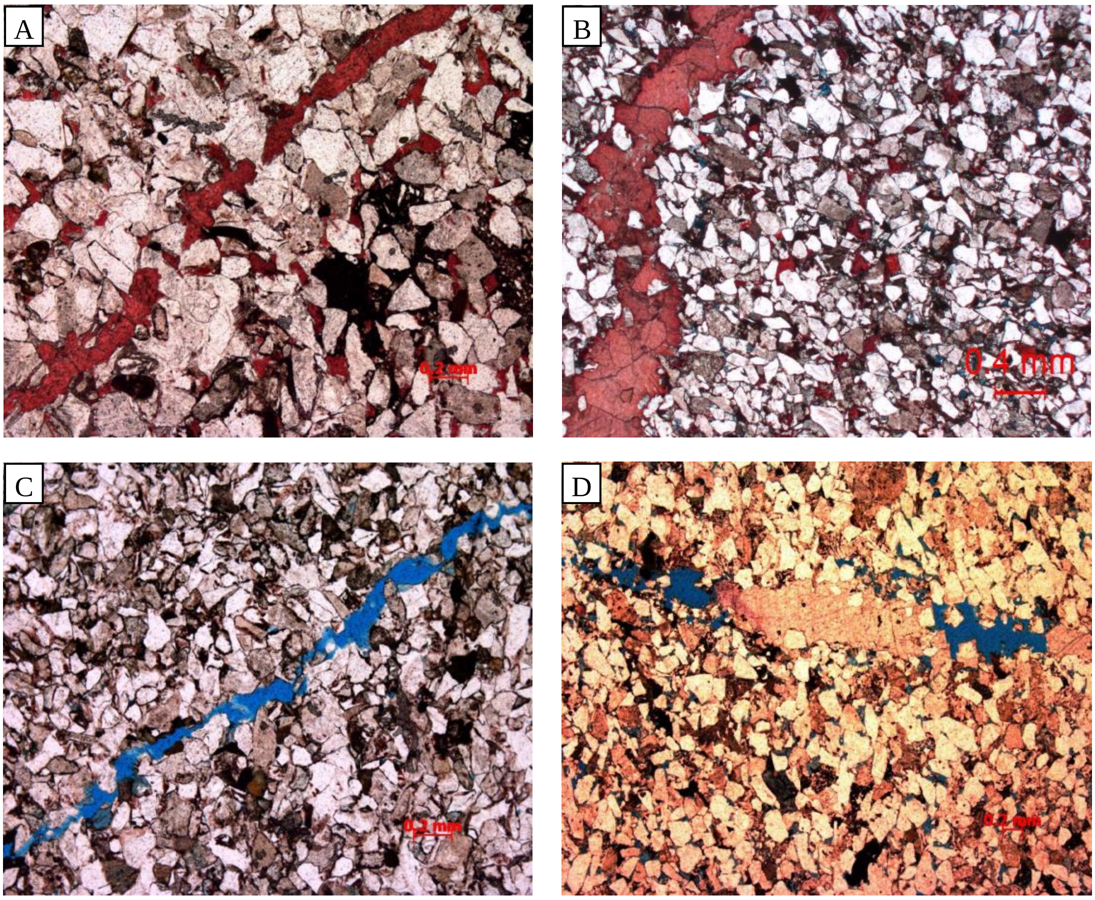

Figure 11. Thin sections showing the cementation and dissolution along the fracture surfaces of Cretaceous Bashijiqike Formation in Kuqa Depression

A. Calcite cementation along fracture surface, Keshen 242, 6567.51 m, K_1*bs*

B. Calcite cementation along fracture surface, Bozi 22, 6323.64m, K_1*bs*

C. Dissolution along fracture plane, Keshen 242, 6568.95 m

D. Coexistence of cementation and dissolution along fracture surfaces, KS 242, 6446.94 m

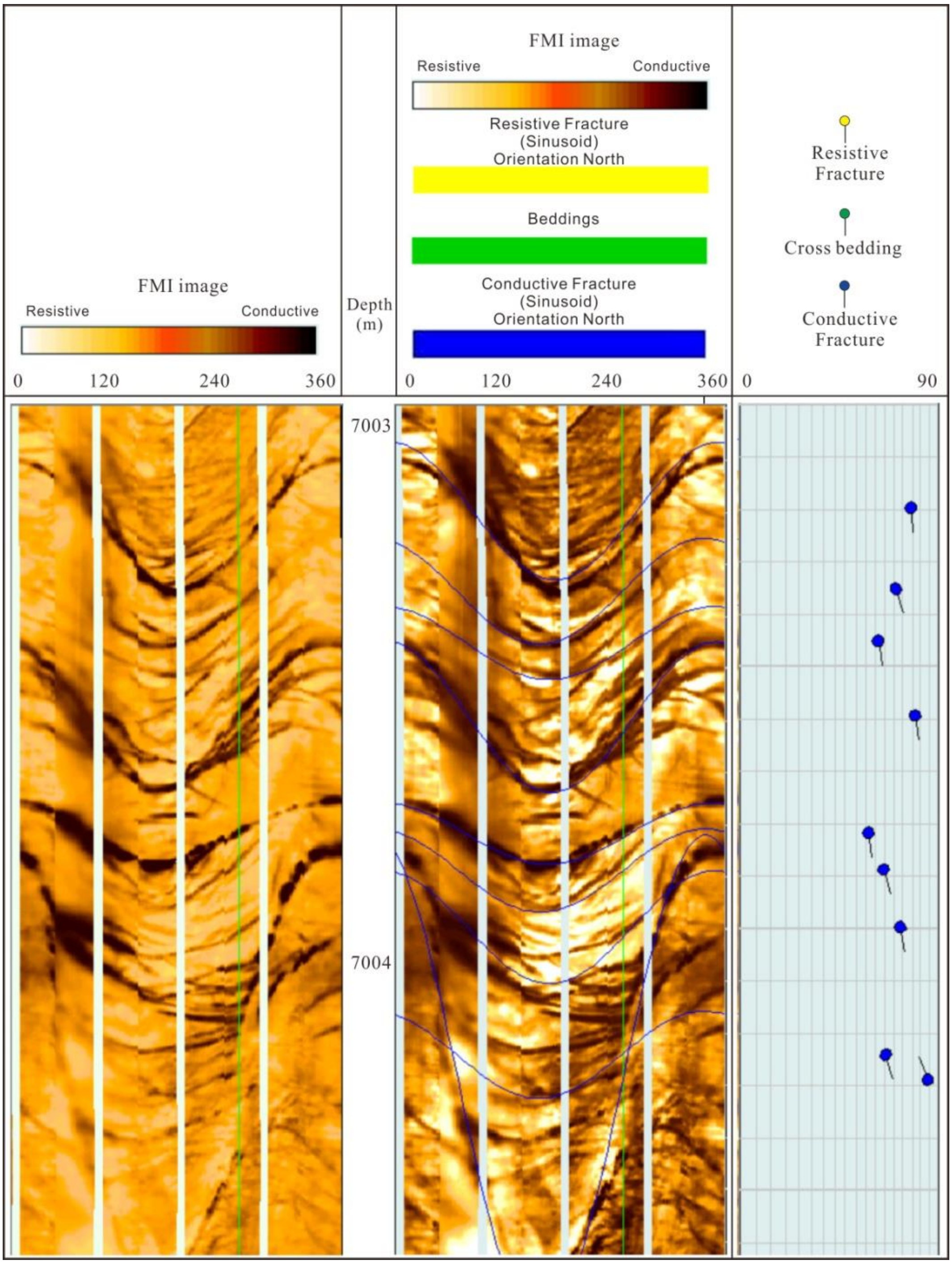

Figure 12. Image logs showing the dissolution along fracture surfaces, forming vuggy fracture of Bashijiqike Formation in Kuqa Depression

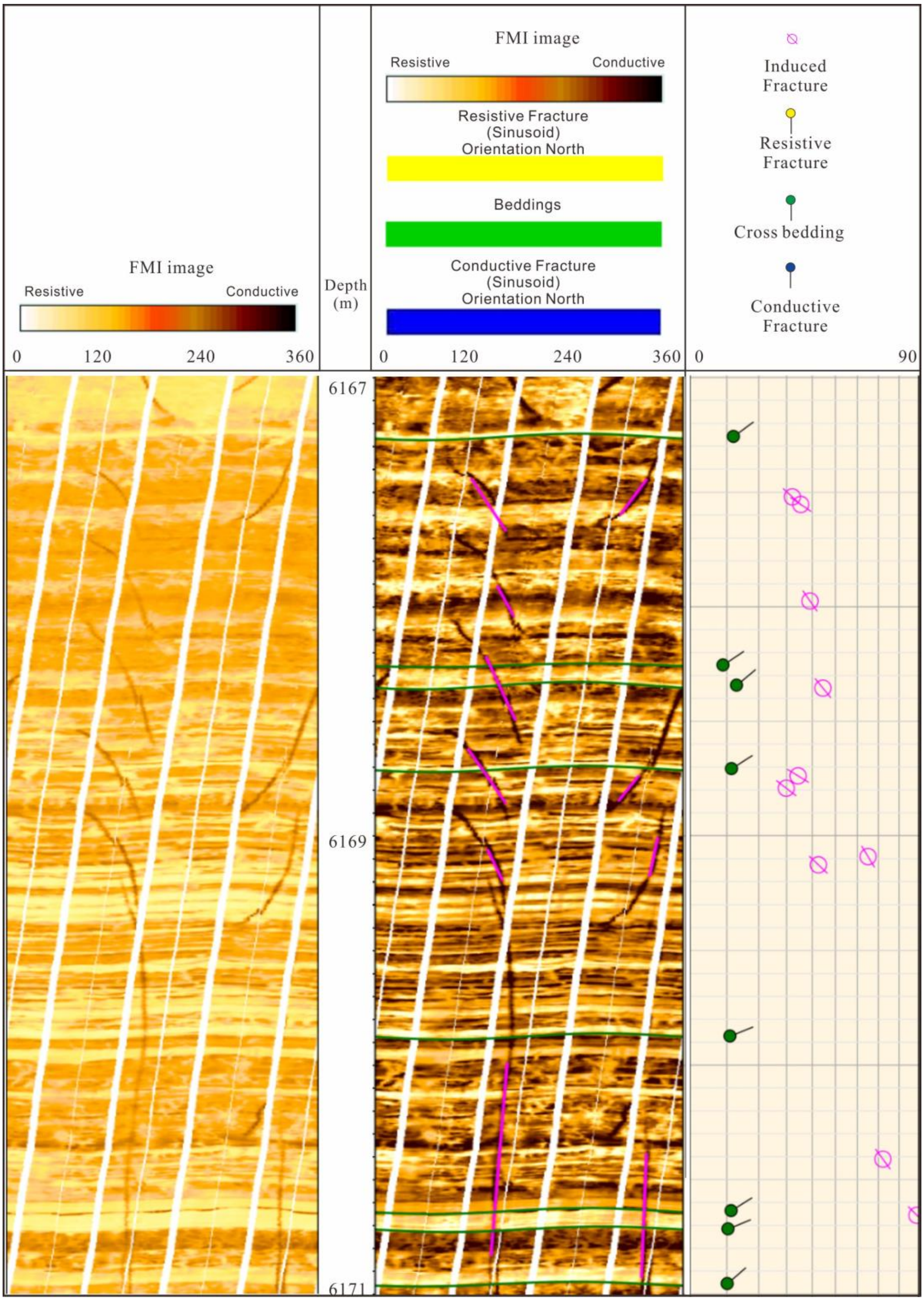

Figure 13. Image logs showing induced fractures indicating the maximum horizontal stress direction (SHmax) of NW-SE

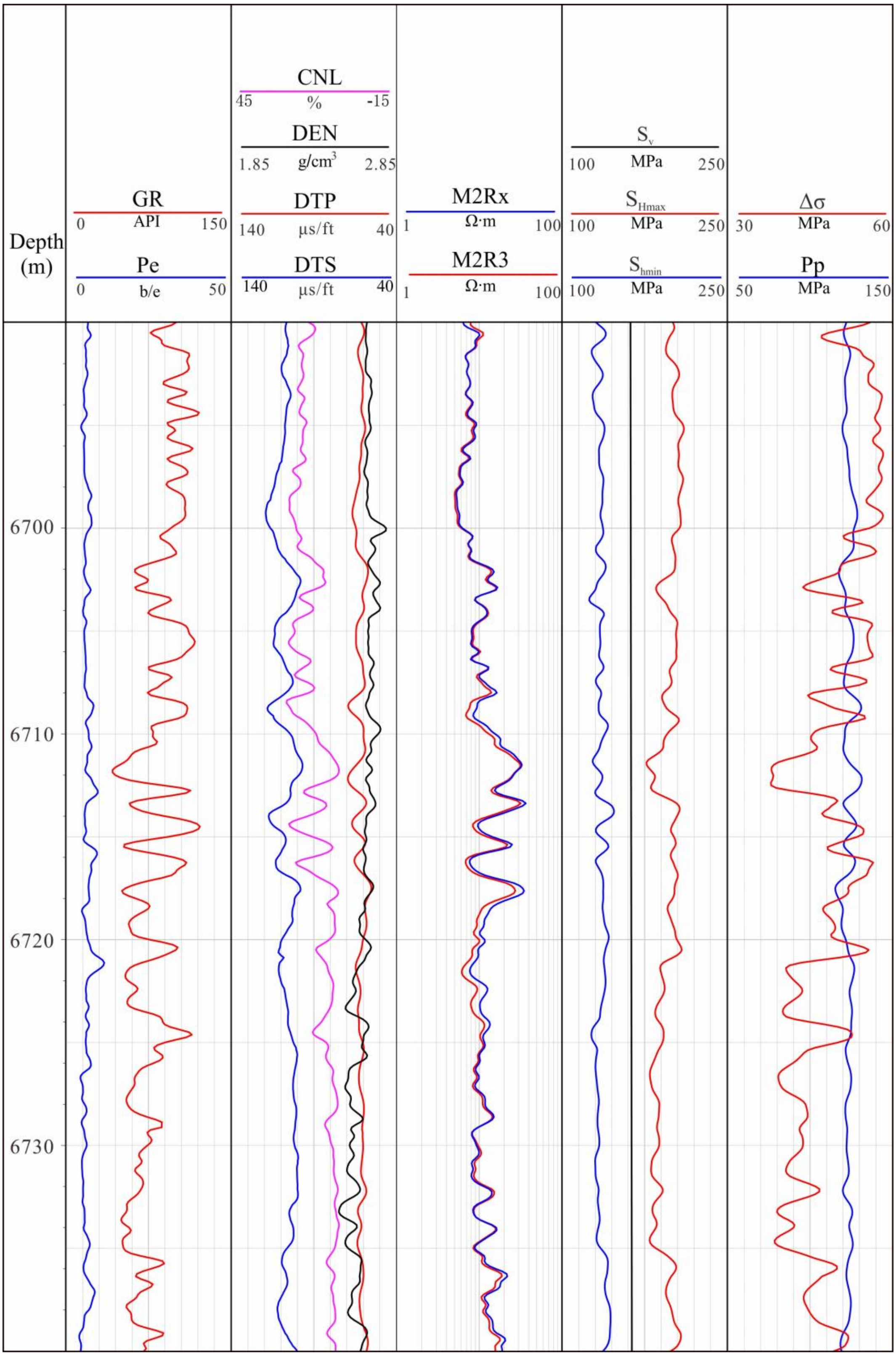

Figure 14. In situ stress magnitude determination via well logs (Keshen 8)

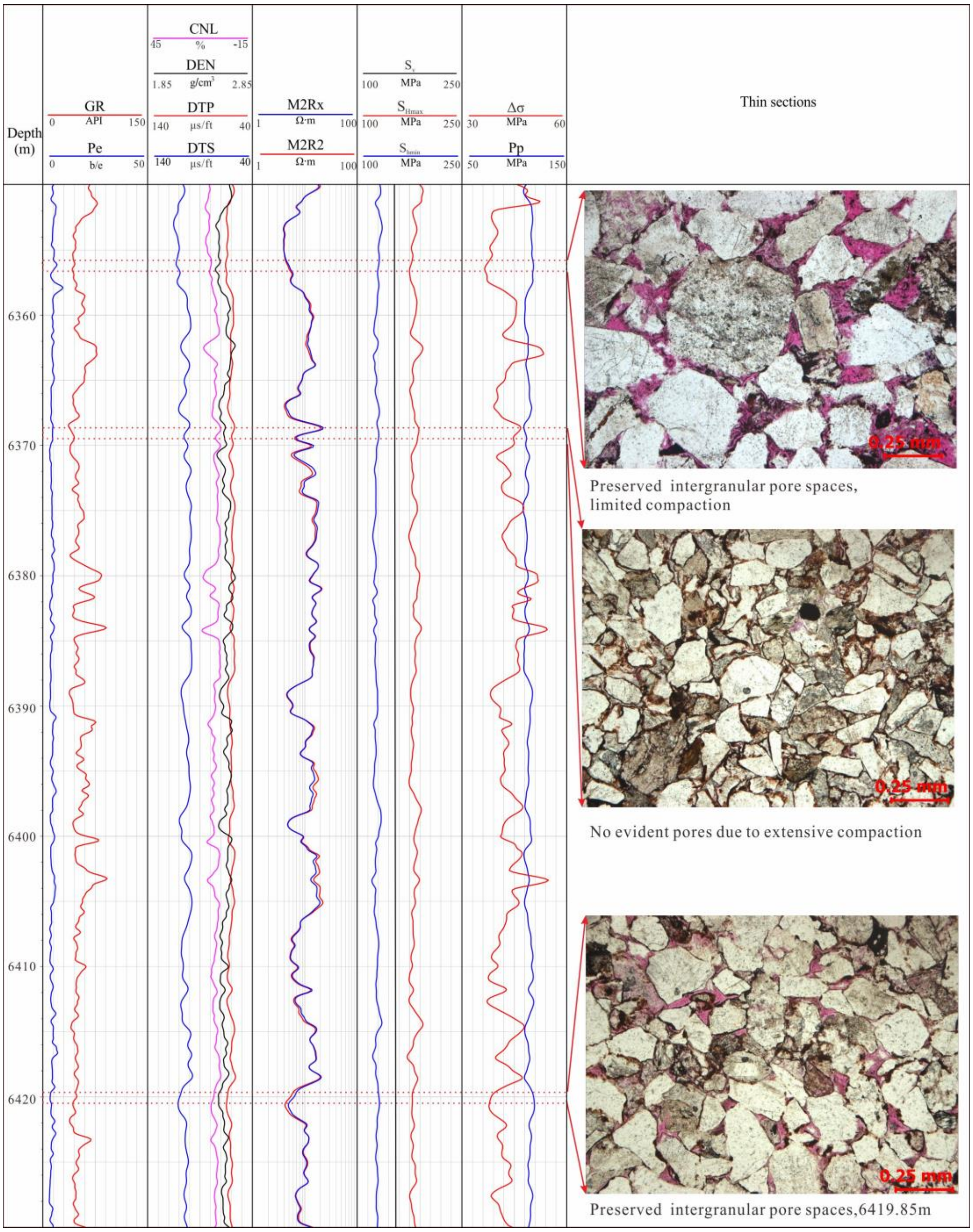

Figure 15. In situ stress magnitude determination via well logs and related thin sections in Well X501

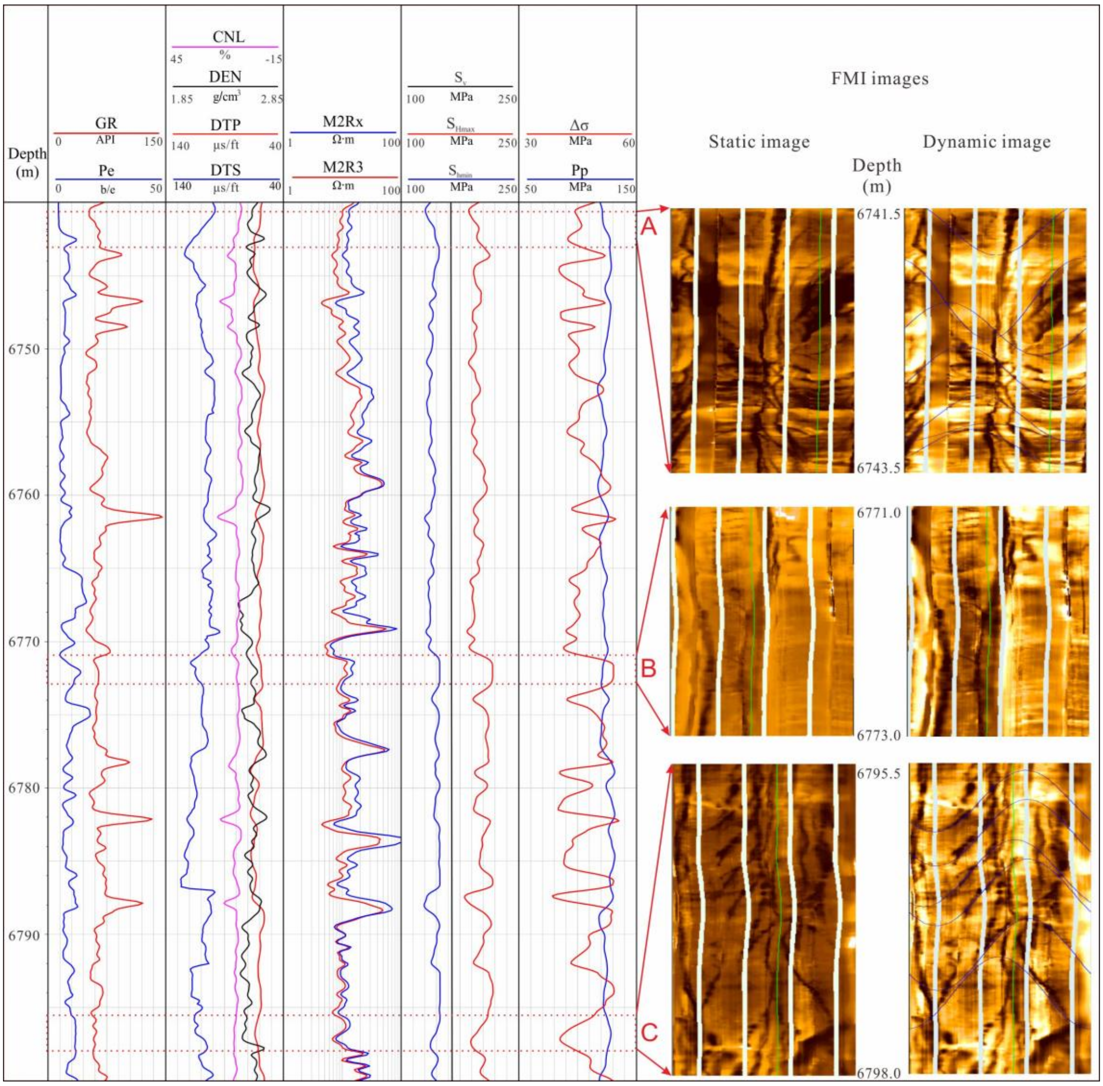

Figure 16. Fracture development within the in situ stress field in Well K8. Note the fractures are related with layers with low horizontal stress differences

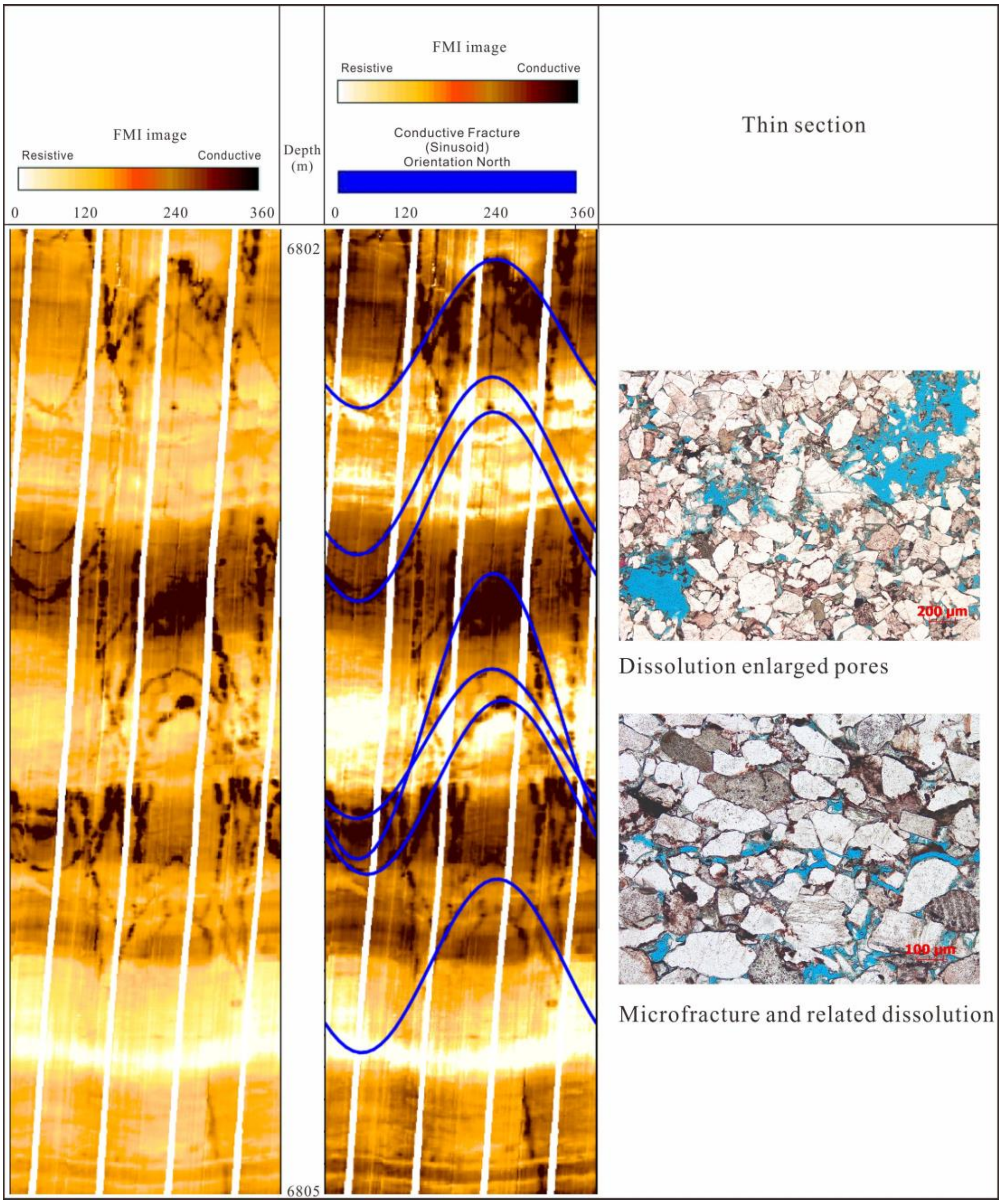

Figure 17. Dissolution pores along fracture surfaces (Bozi 104)

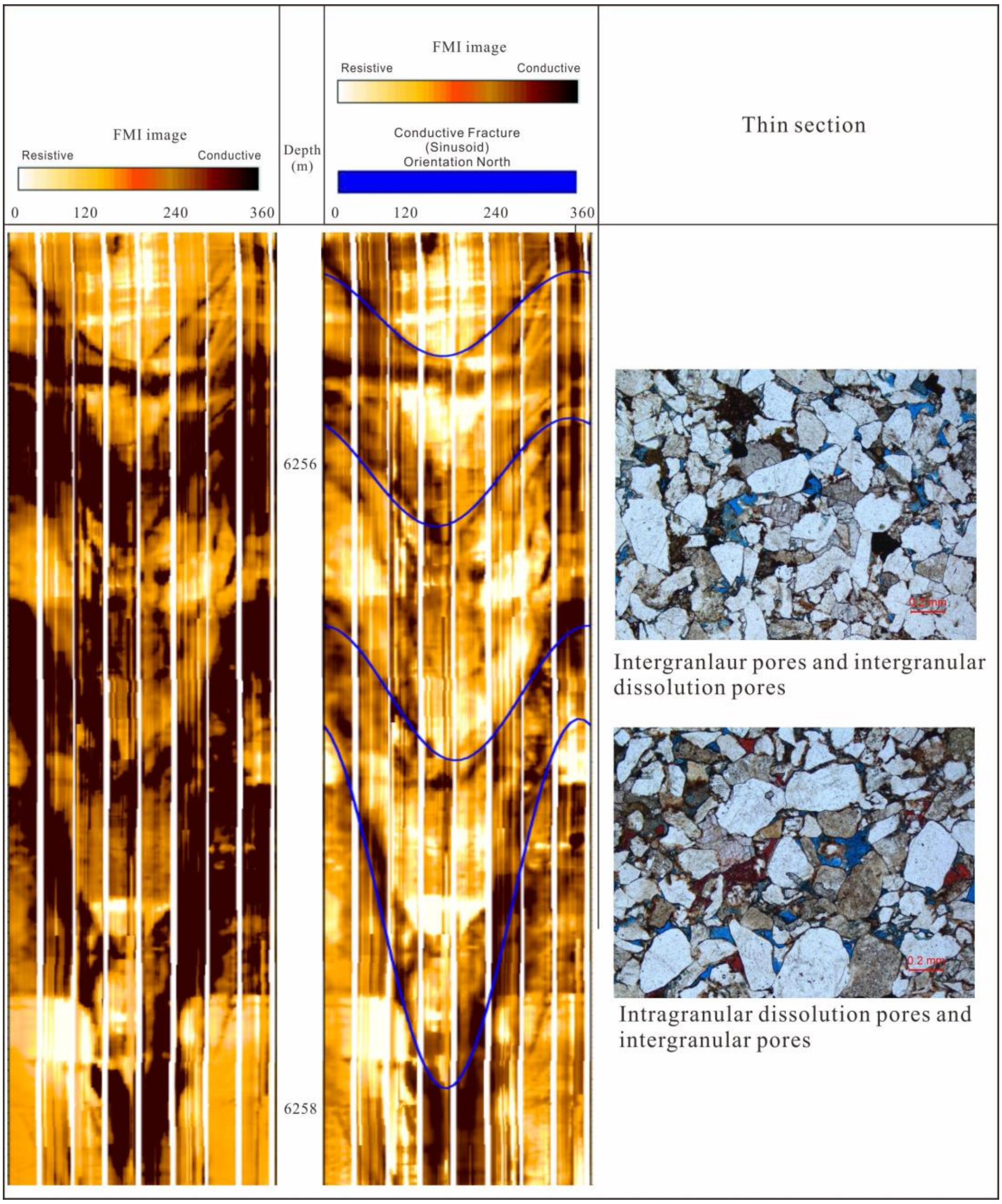

Figure 18. Presences of fracture enhance dissolution and dissolution pores are mainly associated with fractures (Bozi 21)

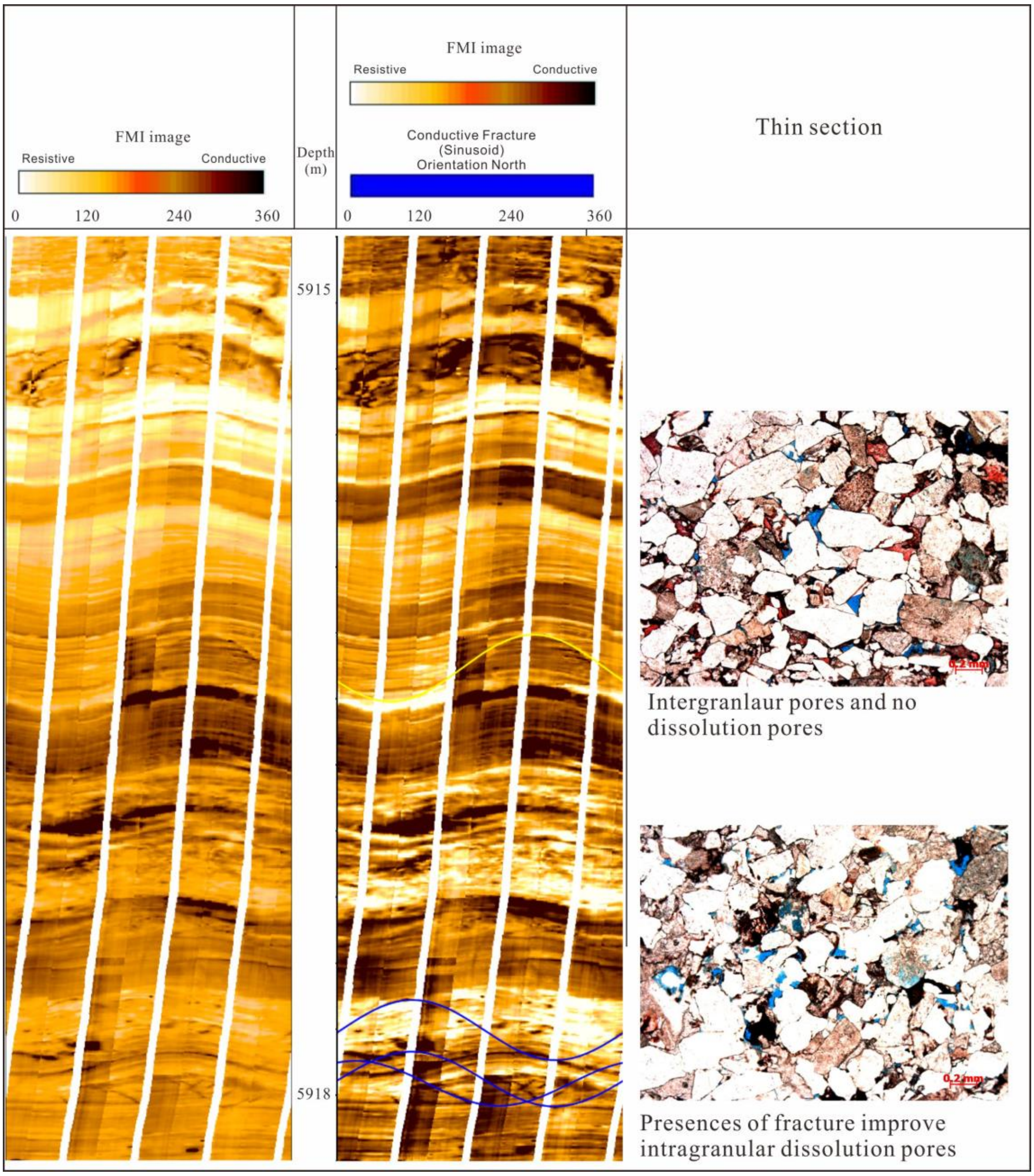

Figure 19. Dissolution pores are mainly associated with fractures, and no evident dissolution pores in layer without fractures (Dabei 1102)

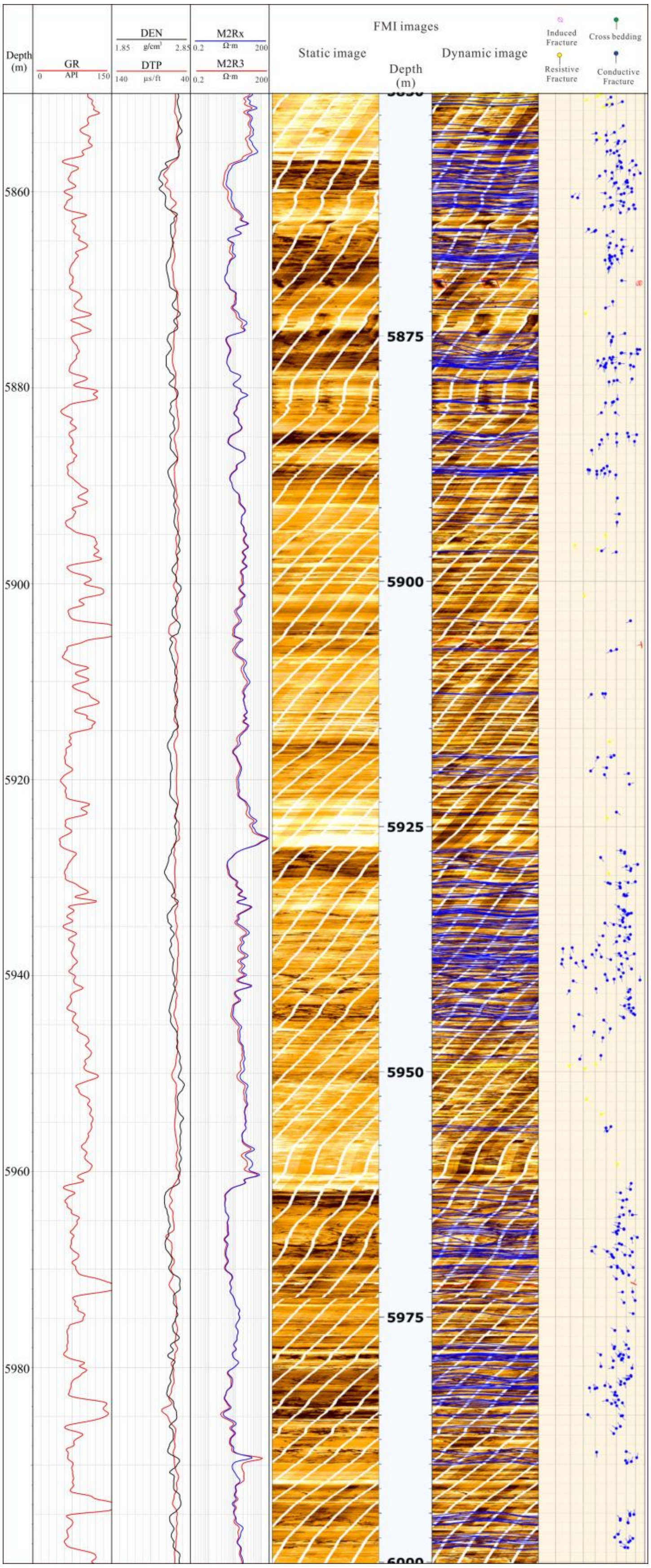

Figure 20. Image log interpreted fractures for Well Dabei 1102

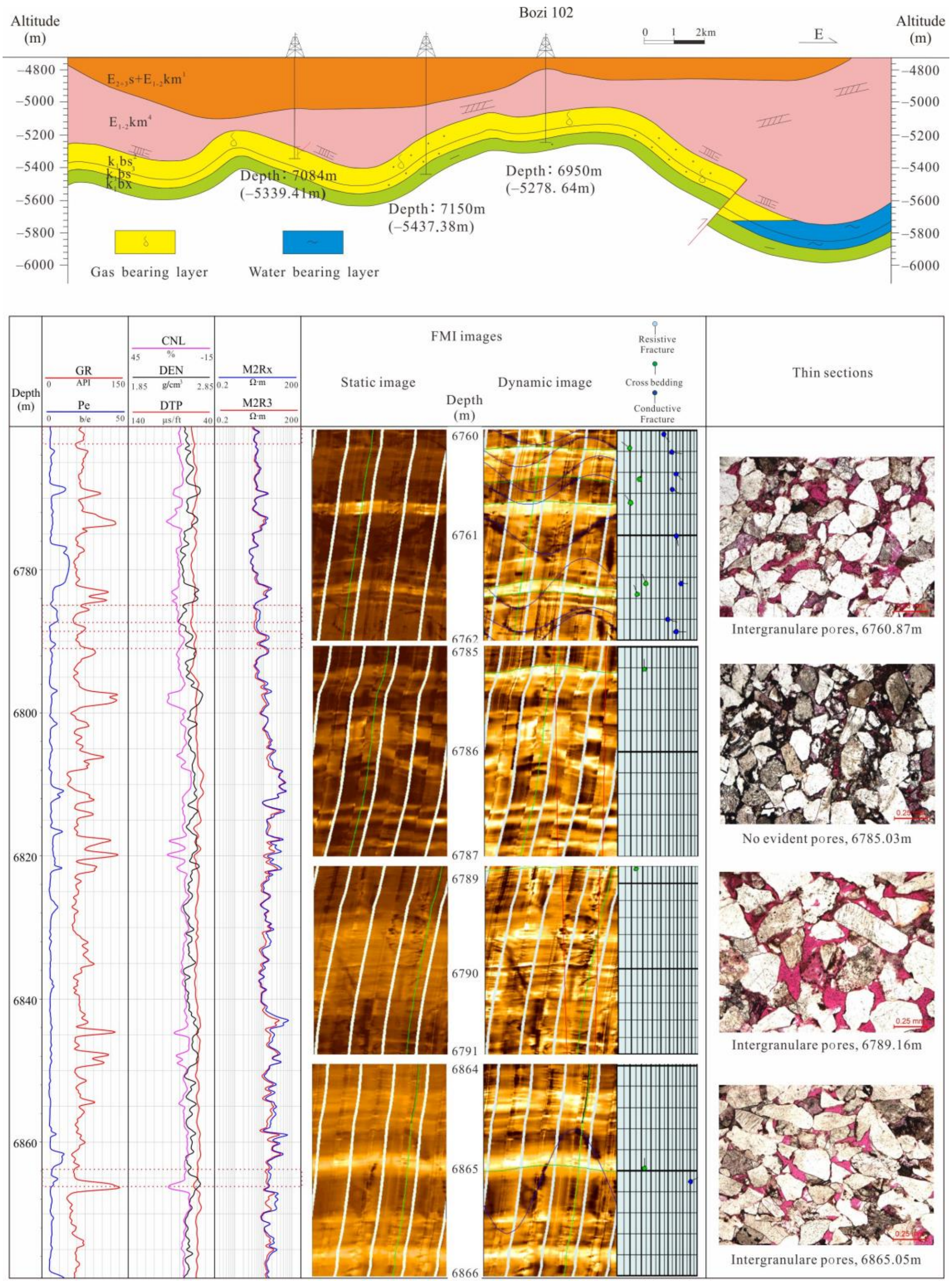

Figure 21. Cross-section of Bozi 1-Bozi 101-Bozi 102 and pore spaces as well as fractures determined from thin section and image logs for Well Bozi 102

Note the dissolution pores associated with fractures, and no evident dissolution pores in layer without fractures.

Well Bozi 102: 6760-6879m depth intervals, 4 mm choke width, the drawdown pressure is 38.41MPa. The daily natural gas production is 106557 m^3.

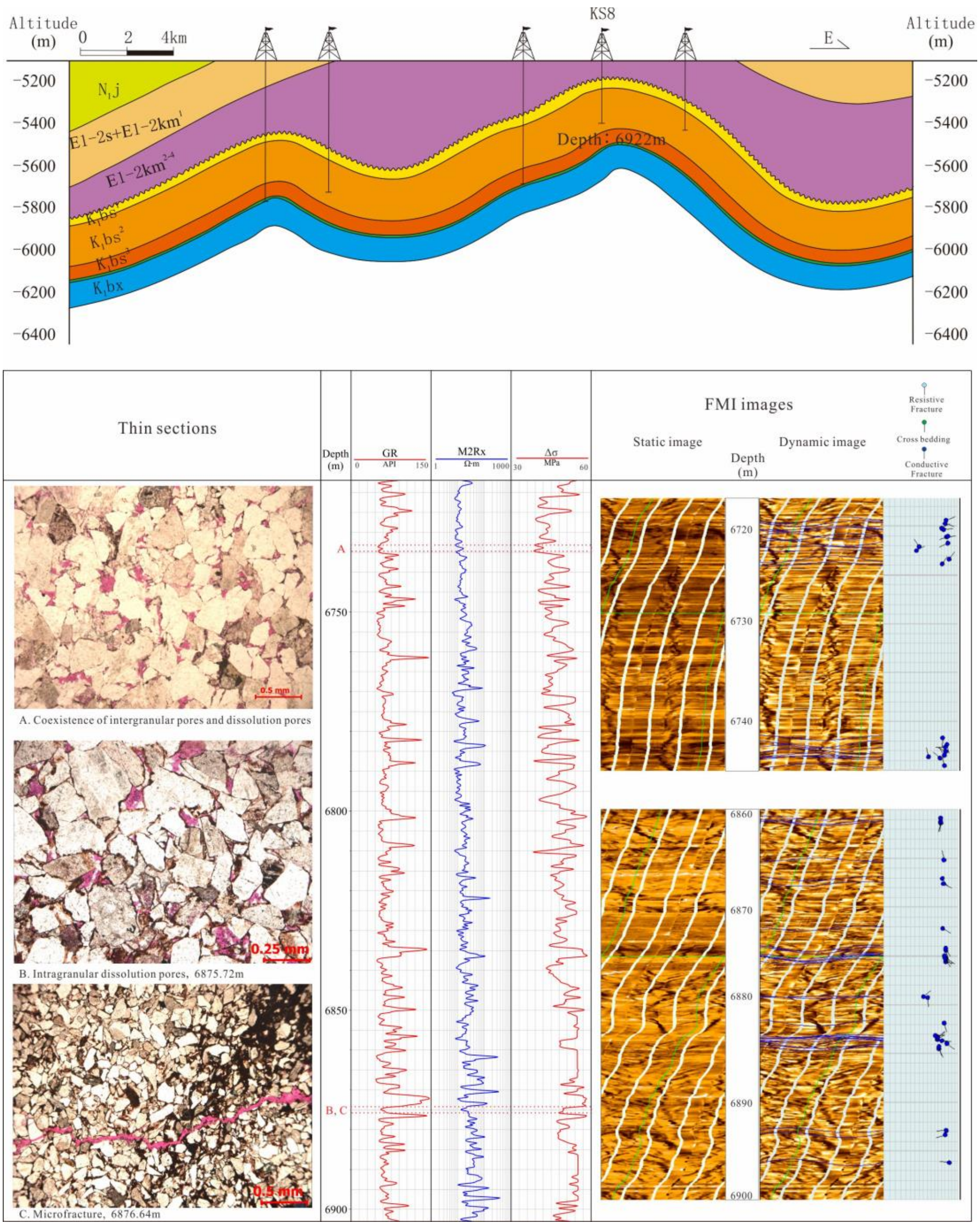

Figure 22. Cross-section of KS 8 and pore spaces as well as fractures interpreted from thin section and image logs for Well KS 8

Note the intergranular pores are associated with low Δσ layers, and dissolution pores coexist with fractures.

Well KS 8: 6717.0-6903.0 m depth intervals, 8 mm choke width, the drawdown pressure is 89.66MPa. The daily natural gas production is 726921 m^3.